The Astrophysical Journal, 811:28 (16pp), 2015 September 20 doi:10.1088/0004-637X/811/1/28

ZFIRE: GALAXY CLUSTER KINEMATICS, Hα STAR FORMATION RATES, AND GAS PHASE METALLICITIES OF XMM-LSS J02182-05102 AT $z_{cl} = 1.6233$*

Kim-Vy H. Tran[1], Themiya Nanayakkara[2], Tiantian Yuan[3], Glenn G. Kacprzak[2], Karl Glazebrook[2], Lisa J. Kewley[3], Ivelina Momcheva[4], Casey J. Papovich[1], Ryan Quadri[1,10], Greg Rudnick[5], Amélie Saintonge[6], Lee R. Spitler[7,8], Caroline Straatman[9], and Adam Tomczak[1]

[1] George P. and Cynthia W. Mitchell Institute for Fundamental Physics and Astronomy, Department of Physics & Astronomy, Texas A&M University, College Station, TX 77843, USA; vy@physics.tamu.edu
[2] Swinburne University of Technology, Hawthorn, VIC 3122, Australia
[3] Research School of Astronomy and Astrophysics, The Australian National University, Cotter Road, Weston Creek, ACT 2611, Australia
[4] Astronomy Department, Yale University, New Haven, CT 06511, USA
[5] Department of Physics and Astronomy, The University of Kansas, Malott Room 1082, 1251 Wescoe Hall Drive, Lawrence, KS 66045, USA
[6] Department of Physics and Astronomy, University College London, Gower Street, London WC1E 6BT, UK
[7] Department of Physics and Astronomy, Faculty of Science and Engineering, Macquarie University, Sydney, NSW 2109, Australia
[8] Australian Astronomical Observatory, P.O. Box 915, North Ryde, NSW 1670, Australia
[9] Leiden Observatory, Leiden University, P.O. Box 9513, NL-2300 RA Leiden, The Netherlands
Received 2015 May 19; accepted 2015 August 11; published 2015 September 16

ABSTRACT

We spectroscopically survey the galaxy cluster XMM-LSS J02182-05102 (hereafter IRC 0218) using LRIS (optical) and MOSFIRE (near-infrared) on Keck I as part of the ZFIRE survey. IRC 0218 has a narrow redshift range of $1.612 < z_{spec} < 1.635$ defined by 33 members of which 20 are at $R_{proj} < 1$ Mpc. The cluster redshift and velocity dispersion are $z_{cl} = 1.6233 \pm 0.0003$ and $\sigma_{cl} = 254 \pm 50$ km s^{-1}. We reach NIR line sensitivities of $\sim 0.3 \times 10^{-17}$ erg s^{-1} cm^{-2} that, combined with multi-wavelength photometry, provide extinction-corrected Hα star formation rates (SFR), gas phase metallicities from [N II]/Hα, and stellar masses. We measure an integrated Hα SFR of $\sim 325\ M_{\odot}$ yr^{-1} (26 members; $R_{proj} < 2$ Mpc) and show that the elevated star formation in the cluster core ($R_{proj} < 0.25$ Mpc) is driven by the concentration of star-forming members, but the *average* SFR per Hα-detected galaxy is half that of members at $R_{proj} \sim 1$ Mpc. However, we do not detect any environmental imprint when comparing attenuation and gas phase metallicities: the cluster galaxies show similar trends with $M_{\star}$ as to the field, e.g., more massive galaxies have larger stellar attenuation. IRC 0218's gas phase metallicity–$M_{\star}$ relation (MZR) is offset to lower metallicities relative to $z \sim 0$ and has a slope of 0.13 ± 0.10. Comparing the MZR in IRC 0218 to the COSMOS cluster at $z = 2.1$ shows no evolution ($\Delta t \sim 1$ Gyr): the MZR for both galaxy clusters are remarkably consistent with each other and virtually identical to several field surveys at $z \sim 2$.

Key words: galaxies: abundances – galaxies: clusters: individual (XMM-LSS J02182-05102) – galaxies: evolution – galaxies: fundamental parameters

1. INTRODUCTION

The advent of sensitive infrared imaging surveys has provided a powerful method for identifying galaxy clusters at $z > 1.5$ (Eisenhardt et al. 2008; Papovich et al. 2010; Gonzalez et al. 2012; Spitler et al. 2012). We are now able to track how clusters build up their galaxy populations over ∼80% of cosmic time ($0 < z < 2.1$). Of particular interest to current galaxy formation models are how scaling relations evolve and depend on environment (Davé et al. 2011a, 2011b; Genel et al. 2014; Tonnesen & Cen 2014; Schaye et al. 2015; Taylor & Kobayashi 2015). For example, the activity observed in clusters at $z > 1$ combined with the old stellar ages of cluster galaxies at $z \sim 0$ indicate that $1 < z < 2$ is an important epoch for understanding how star formation is quenched (e.g., Rudnick et al. 2012; Brodwin et al. 2013).

Essential to measuring scaling relations at $z \sim 2$ is separating first cluster galaxies from the field. IR imaging is effective at identifying galaxy overdensities at $z > 1.5$, but broadband photometric redshifts (z_{phot}) are coarse and field contamination is a concern, especially beyond the cluster core.[11] This is also true for studies using narrow-band imaging to identify Hα-emitting members (Finn et al. 2005; Koyama et al. 2013a). Neither method can measure cluster kinematics, and both are susceptible to contamination by broad-line active galactic nuclei (AGNs). While *Hubble Space Telescope* (*HST*) WFC3 grism observations can measure continuum features, e.g., the Balmer break, as well as strong emission lines (Brammer et al. 2012; Gobat et al. 2013; Zeimann et al. 2013; Newman et al. 2014), the spectral resolution is too low for measuring cluster kinematics and spectral lines such as Hα and [N II] are blended. The WFC3 footprint also is limited to the cluster core.

Due to these limitations, currently there are only four (proto) galaxy clusters at $z > 1.5$ that have enough members ($\gtrsim 15$) for a kinematic analysis (Bayliss et al. 2014; Shimakawa et al. 2014; Yuan et al. 2014). The large range in measured cluster velocity dispersions (550–1500 km s^{-1}) and substantial spatial substructure confirm that these are dynamically young systems. Because the $z \sim 1.5$–2 clusters are still assembling, we can better disentangle evolution driven by environment versus galaxy mass (Peng et al. 2010; Muzzin et al. 2012; Papovich et al. 2012; Quadri et al. 2012; Wetzel et al. 2012; Bassett

* http://zfire.swinburne.edu.au
[10] Mitchell Postdoctoral Fellow.
[11] Although see results using medium-band NIR filters that improve z_{phot} by a factor of ∼5 compared to broadband measurements (Whitaker et al. 2011; Spitler et al. 2012)

et al. 2013). For example, the discovery of intense star formation in the cluster cores (Hilton et al. 2010; Tran et al. 2010; Zeimann et al. 2013) suggests an active interplay between enrichment of gas in the inter-stellar medium (ISM) and the intra-cluster medium.

The primary challenge to studying cluster galaxy populations at $z > 1.5$ is the need for near-IR spectroscopy. With the installation of efficient multi-object near-IR spectrographs such as *Subaru*/FMOS (Kimura et al. 2010), Very Large Telescope/KMOS (Sharples et al. 2013), and Keck/MOSFIRE (McLean et al. 2012), we can now obtain key rest-frame features from [O II]λ3727, 3729 Å to [S II]λ6717, 6731 Å for galaxy clusters at $z > 1.5$. These spectral features have been used to establish empirical scaling relations at $z \sim 0$ that we can now test at $z \sim 2$, i.e., can we detect an environmental dependence in addition to redshift evolution?

The increasing activity in galaxy clusters with redshift raises the question of how star formation rates (SFR), stellar masses ($M_\star$), attenuation, and gas phase metallicities are related. Star-forming cluster galaxies at $z > 1$ define a SFR–$M_\star$ relation similar to the field ("main sequence"; Daddi et al. 2007; Noeske et al. 2007; Koyama et al. 2013b), but studies suggest there are environmental differences, e.g., suppressed star formation in low-mass members and less attenuation (Zeimann et al. 2013). If cluster galaxies follow a different relation between specific SFR (SSFR) and stellar mass (SSFR–$M_\star$), this could mean that the ionization conditions are also different (Kewley et al. 2015).

Recent studies of gas phase metallicity versus $M_\star$ (MZR) find that galaxies at $z \sim 2$ are uniformly offset from the local relation (Erb et al. 2006a; Steidel et al. 2014; Sanders et al. 2015). However, while the MZR in the local universe shows an environmental dependence, (Cooper et al. 2008; Ellison et al. 2009; Peng & Maiolino 2014), it is unclear if this is also the case at $z \sim 2$: several studies using stacked spectra find the cluster galaxies to be more metal-rich than their field counterparts (Kulas et al. 2013; Valentino et al. 2014; Shimakawa et al. 2015), but Kacprzak et al. (2015) study ~50 cluster galaxies at $z = 2.1$ and find no difference from the field.

To determine if empirical relations vary with environment at $z \sim 2$, the ZFIRE survey combines NIR spectroscopy obtained with Keck/MOSFIRE (McLean et al. 2012) with deep multi-wavelength imaging to study cluster galaxies at $z \sim 2$. We compare to field measurements obtained by complementary surveys such as KBSS (Steidel et al. 2014) and MOSDEF (Kriek et al. 2015). Initial ZFIRE results on the COSMOS cluster at $z = 2.1$ (Spitler et al. 2012) include spectroscopically confirming >50 members and measuring the cluster's velocity dispersion (Yuan et al. 2014), measuring the cluster's gas phase metallicity–$M_\star$ relation (Kacprzak et al. 2015), and investigating the ionization properties of the ISM of individual cluster galaxies (Kewley et al. 2015).

As part of our ZFIRE survey, we obtain optical and NIR spectroscopy of XMM-LSS J02182-05102 (hereafter IRC 0218)[12] at $z_{cl} = 1.6233$. Originally reported by Papovich et al. (2010), IRC 0218 was one of the first galaxy clusters to show an increasing fraction of star formation with increasing local density (Tran et al. 2010). Estimates of IRC 0218's total SFR as determined by IR observations are >1000 $M_\odot$ yr^{-1} (Popesso et al. 2012; Santos et al. 2014). Because IRC 0218 is still in the process of building its galaxy population (Rudnick et al. 2012), the cluster is an ideal target for tracking how star formation, gas phase metallicities, and dust vary with stellar mass as a function of environment at $z > 1.5$.

In our analysis, we center IRC 0218 on the Brightest Cluster Galaxy (BCG) at $(\alpha, \delta)_{J2000} = (02{:}18{:}21.5, -5{:}10{:}19.9)$. The BCG is also currently the most distant galaxy–galaxy lens with a total mass within the Einstein radius of $1.8 \times 10^{11}\ M_\odot$(Wong et al. 2014). We use a Chabrier Initial Mass Function and AB magnitudes throughout our analysis. We assume $\Omega_m = 0.7$, $\Omega_\Lambda = 0.3$, and $H_0 = 70$ km s^{-1} Mpc^{-1}. At $z = 1.62$, the angular scale is $1'' = 8.47$ kpc.

2. OBSERVATIONS AND DATA

2.1. Target Catalog

Spectroscopic targets were selected from the Williams et al. (2009) catalog of the Ultra-deep Survey (UDS) taken as part of the UKIRT Infrared Deep Sky Survey (UKIDSS), a public near-infrared imaging survey (Lawrence et al. 2007). The K-selected catalogs reach 5σ-limiting magnitudes in a $1''.75$ diameter of $B_{AB} < 27.7$, $R_{AB} < 27.1$, $i_{AB} < 26.8$, $z_{AB} < 25.5$, $J_{AB} < 23.9$, and $K_{AB} < 23.6$ mag. We refer the reader to Williams et al. (2009) and Quadri et al. (2012) for more details on the photometric and z_{phot} catalogs used in this work.

2.2. Optical Spectroscopy: Keck/LRIS

Using the LRIS (Oke et al. 1995, $5'.5 \times 8'$ field of view; $0''.135$ per pixel) on Keck, we carried out a spectroscopic survey centered on the cluster on 2012 October 19 and 20 (NASA/Keck Program ID 48/2012B). The primary LRIS targets were selected to be brighter than $i_{AB} = 21$ mag and the secondary targets (mask fillers) between $21 < i_{AB} < 24$ mag. No morphological selection was applied. Of the primary targets, higher priority was also given to objects identified to be candidate star-forming cluster galaxies (Tran et al. 2010), candidate Lyman-break Galaxies at $z_{phot} > 1.35$, and [O II]-emitters identified from narrow-band imaging (Tadaki et al. 2012).

We use the 600/4000 grism for the blue side of LRIS ($0.38 < \lambda < 0.58\ \mu$m and the 600/10000 grating for the red side ($0.70 < \lambda < 1.0\ \mu$m; with $1''$ slit widths, the corresponding resolution is 4.0 Å and 4.7 Å respectively. Observing conditions were excellent with median seeing of about $0''.6$. A subset of high priority targets, e.g., the BCGs, were targeted in three of the four observed masks. For masks 1, 2, and 3 which included common high priority targets, we obtained 9×20 minute exposures. For mask 4 which included a more general redshift selection, we obtained 5×20 minute exposures. The four LRIS masks have a total of 136 targets including repeats. For all the exposures, we dithered by $\pm 1''$ along the slit to minimize sky residuals. Standard calibrations including flat-fields and arc lamps (ArCdHgNeZn) for each mask also were taken.

To reduce the spectra, we follow Tran et al. (2007) and use IRAF[13] routines with custom software provided by D. Kelson (Kelson 1998, 2003). To summarize, we first convert the multi-

[12] This galaxy cluster is also referred to as CLG0218.3-0510 by Tran et al. (2010) and Santos et al. (2014).

[13] IRAF is distributed by the National Optical Astronomy Observatories, which are operated by the Association of Universities for Research in Astronomy, Inc., under cooperative agreement with the National Science Foundation.

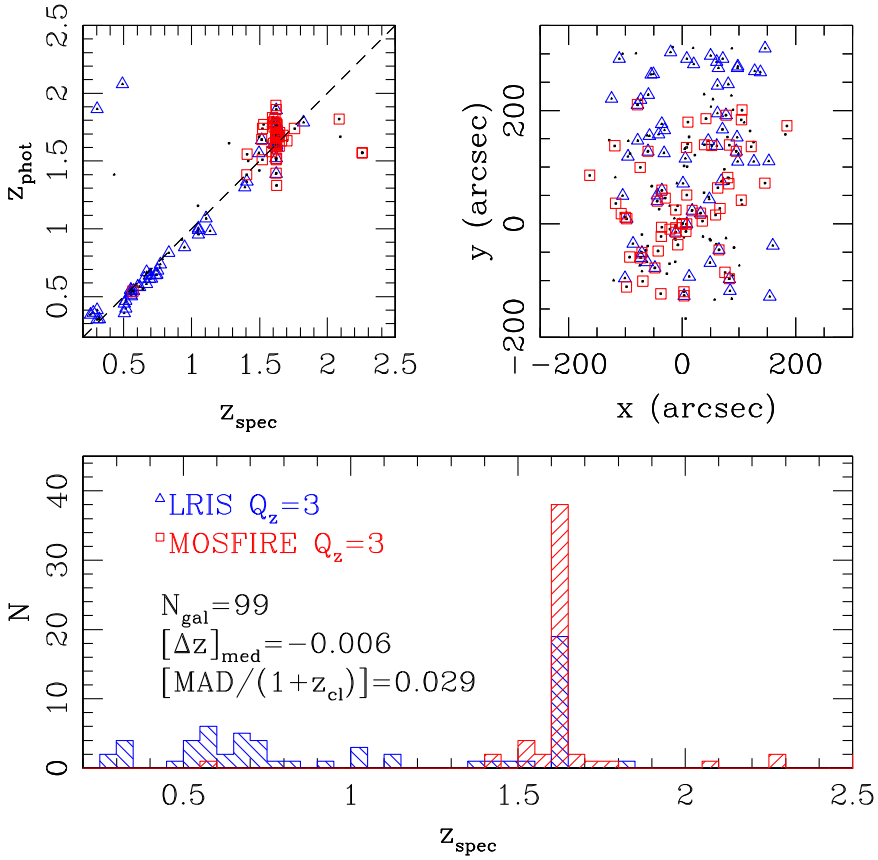

Figure 1. Photometric redshifts from Williams et al. (2009) compared to spectroscopic redshifts for all objects with measured redshifts (top left; the dashed diagonal line denotes parity) and their spatial distribution (top right). Objects with $z_{\rm spec}$ quality flag of $Q_z = 3$ are shown as open blue triangles (LRIS) and open red squares (MOSFIRE). Note that ∼30 objects have $z_{\rm spec}$ from both spectrographs. The bottom panel shows the $z_{\rm spec}$ histograms for LRIS (blue) and MOSFIRE (red) for objects with $Q_z = 3$.

extension files into single images for the blue and red sides; we reduce the blue and red sides of LRIS separately. Cosmic rays are particularly problematic on the red side and we remove as many as possible using *crutil* in IRAF; the blue side is minimally affected by cosmic rays. We flat-field the science frames, determine the vacuum wavelength solution with the arclamp, remove the sky lines, and rectify the 2D spectra. We median the rectified science frames for each mask to obtain a single combined image.

The 2D spectra first were visually inspected to identify all potential sources including emission-line only objects. The 1D spectra were extracted by summing the five rows centered on the source (0.″135 per pixel) of each 2D spectrum; the wavelength coverage for the extracted spectra is 3800–5800 Å (blue side) and 7000–10000 Å (red side). For galaxies at $z \sim 1.6$, this corresponds to rest-frame UV where the continuum is detected for only a handful of systems. To measure redshifts, we use *xcsao* in IRAF (Kurtz et al. 1992) with various templates for star-forming, quiescent, post-starburst, Lyman-break, and Lyα galaxies; we refer the reader to Tran et al. (2005b) for details.

2.3. Near-infrared Spectroscopy: Keck/MOSFIRE

At $z_{\rm cl} = 1.6233$, most of the rest-frame optical spectral features such as Hβ and Hα have shifted to the near-IR. To measure these features and provide continuous spectral coverage of the cluster galaxies, we used Keck/MOSFIRE (McLean et al. 2012) on 2013 December 23 and 24 and on 2014 February 10–13. Primary targets were galaxies spectroscopically confirmed with the LRIS observations to be at $z > 1.5$ (see Figure 1). We also included objects from the 3D-*HST* survey with grism redshifts $z > 1.5$ (I. Momcheva et al. 2015, in preparation). Secondary targets were selected to have $z_{\rm phot} > 1.4$ using the Williams catalog, and the lowest priority fillers had $z_{\rm phot} < 1.4$ and $i_{\rm AB} < 22$ mag.

We obtained YJH spectroscopy corresponding to wavelength ranges of 0.97–1.12 μm, 1.15–1.35 μm, and 1.46–1.81 μm respectively. Using 0.″7 slit-widths (pixel scale is 0.″18), the spectral resolution of $R \sim 3600$ corresponds to a dispersion of 1.086, 1.303, and 1.627 Å/pixel for YJH. The MOSFIRE spectroscopic field of view is $3' \times 6'$, and we observed four masks with approximately 25–35 objects targeted in each to map the galaxy cluster (Figure 1). All the masks were designed using the MAGMA slitmask design software.[14] A slit star was included in each mask to monitor the flux throughput and seeing. Flat-fields and arcs (Neon, Argon) were taken during afternoon calibrations for each mask.

For the 2013 December run, we designed three masks that were observed with both J and H. The seeing FWHM on the first night was ∼0.″7–0.″9 and improved to ∼0.″6 on the second night. Adjusting for the seeing conditions to reach approximately the same flux limit in all masks, we integrated for a total of 2880–3360 s and 2880–5880 s in the J and H bands,

[14] www2.keck.hawaii.edu/inst/mosfire/magma.html

respectively; individual exposure times for both JH bands were 120 s. All spectroscopy was taken with an ABBA dither pattern and an offset of 2.″5. Long-slit spectroscopy of the standard star Feige 15 was taken on both nights to correct for telluric absorption by the atmosphere and to flux calibrate the data.

For the 2014 February run, we used a single mask to obtain Y band spectroscopy of mostly confirmed cluster members. Conditions on the first night were poor with seeing FWHM of 1.″2 (none of these observations are usable) but improved to ∼0.″7–0.″9 for the following three nights. The Y mask was observed each night for 5040–6660 s with individual exposure times of 180 s. The total integration time is 24,300 s, but we note that useful time on target is less due to varying conditions on the first two nights. Data taken under poorer weather conditions were given less weight when combining the observations, i.e., the data were weighted by the signal-to-noise ratio (S/N) of the continuum.

To reduce the MOSFIRE spectroscopy, we use the publicly available data reduction pipeline (DRP) developed by the instrument team.[15] The DRP provides background-subtracted, rectified, and (vacuum) wavelength calibrated 2D spectra for each slit. Using custom IDL routines, we then correct the 2D spectroscopy for telluric absorption and flux calibrate using the standard star observations. To extract the 1D spectra and associated 1σ error spectra, we fit a Gaussian profile along the spatial direction to determine the extraction aperture for each object; typical extraction apertures are $\sim 1''$. For objects that are too faint to fit a spatial profile, we use the Gaussian profile fit to the slit star in the same mask.

The 2D spectra were visually inspected to identify all potential sources; for the most part, these detections are emission lines, e.g., Hα in the H-band for galaxies at $z \sim 1.6$. Spectroscopic redshifts were determined with two-step method: (1) using *xcsao* in IRAF with an emission-line template and, where possible, combining JH observations, to measure a redshift and (2) using this redshift to fit 1D Gaussians to emission lines along the spectral direction and propagating errors using the corresponding error spectrum.

For more details on our data reduction, we refer to our MOSFIRE analysis of the COSMOS cluster (Yuan et al. 2014). Especially thorough reviews of MOSFIRE observing strategies and data reduction are also presented by Kriek et al. (2015) and Steidel et al. (2014); note that the latter uses the public DRP released for MOSFIRE. Both publications provide extensive discussion on the capabilities of the instrument and strategies for post-processing. A full description of our data reduction for IRC 0218 and the COSMOS galaxy cluster at $z = 2.1$ also will be presented in T. Nanayakkara et al. (2015, in preparation).

2.4. Redshift Catalog

Each spectroscopic redshift is assigned a quality flag Q_z where $Q_z = 3$ denotes a robust measurement (multiple spectral lines), $Q_z = 2$ is likely (single spectral line with potential secondary line), and $Q_z = 1$ is guess (single line and/or no strong spectral features). The combined spectroscopic observations from LRIS and MOSFIRE yield 130 unique redshifts. Note that all of the cluster galaxies reported here are confirmed with emission-lines, e.g., the split [O II]λ3727 Å doublet or Hα+[N II] pair. Faint continua are detected for only a handful of cluster galaxies and are not reliable for measuring absorption-line redshifts, i.e., our survey is strongly biased toward active galaxies with emission lines. In our analysis, we use only the 109 unique objects with redshift quality flag of $Q_z = 3$ (54 identified by LRIS and 55 by MOSFIRE).

We find the spectroscopic redshifts are in good agreement with the photometric redshifts (Figure 1, top left). The $z_{\rm phot}$–$z_{\rm spec}$) distribution for the 99 objects with $z_{\rm spec} > 0$ and $Q_z = 3$ has a median difference of $[\Delta z]_{\rm med} = -0.006$; we use the median to minimize the effect of redshift outliers. The corresponding absolute median deviation is ∼3% where the latter is determined using $\Delta z/(1 + z_{\rm spec})$ and assuming $z_{\rm spec} = 1.62$. For the 49 galaxies at $1.5 < z_{\rm spec} < 1.7$, the median difference is 0.06 and absolute median deviation is also ∼3%; there is only one spectroscopically confirmed member with $|z_{\rm phot}-z_{\rm spec}| > 0.3$.

The redshift distributions in Figure 1 (bottom) demonstrate how well LRIS and MOSFIRE complement each other. LRIS is effective up to $z \sim 1.6$ because [O II] is still within the LRIS wavelength range. MOSFIRE is extremely effective at $z > 1.5$ when [O III] and Hα move into the J and H bands, respectively.

2.5. NIR Emission-line Fluxes

To obtain spectro-photometric data and correct for the slit-loss, we flux calibrate the MOSFIRE observations using a combination of ground-based and *HST* imaging. We use the standard star flux calibrated data from our custom IDL routines to compare with the data from the (publicly) available UKIDSS Data Release 8 (Quadri et al. 2012). More information on the filter systems used in UKIDSS can be found in Hewett et al. (2006).

We mask the sky regions in the spectra by assigning them weights of zero and use an inverse variance weighting to calculate the total spectroscopic fluxes for each 1D spectrum. We use the UKIRT WFCAM filter response functions to be able to directly compare our results with the total broadband photometric fluxes of UKIDSS.

For each MOSFIRE mask in a given band, we calculate the median offset between the spectroscopic magnitudes and the broadband photometric magnitudes for all objects brighter than 23 mag. We use the median offset as the correction factor to be applied to all the objects in the respective masks to account for slit losses. We then calculate the normalized median absolute deviation (MAD) for objects with a broadband magnitude brighter than 24 mag to determine the uncertainty for the scaling process. We find the J-band to have systematically more scatter compared to the H-band. We calculate the flux uncertainties in the calibrated spectra to be ∼20%. A more detailed analysis will be presented in T. Nanayakkara et al. (2015, in preparation).

Our analysis uses H$\alpha\lambda$6563 Å, H$\beta\lambda$4861 Å, [N II]λ6583 Å, and [O III]λ5007 Å line fluxes to measure redshifts, SFR, gas attenuation, and gas metallicities of $z \sim 1.6$ galaxies. Hα is the strongest emission line and falls in the H-band; all of the Hα detections are measured at $>4\sigma$ significance for these galaxies. We identify 45 galaxies at $1.58 < z_{\rm spec} < 1.68$ (Figure 2) with Hα fluxes of $(0.6–16.5) \times 10^{-17}$ erg s^{-1} cm^{-2}. The H-band includes the much weaker [N II] emission line; objects with [N II] measurements that are below the detection limit of $\sim 0.3 \times 10^{-17}$ erg s^{-1} cm^{-2} and/or detected with statistical significance of $<2\sigma$ are assigned 1σ upper limits from the line-fitting.

[15] https://github.com/Mosfire-DataReductionPipeline/MosfireDRP

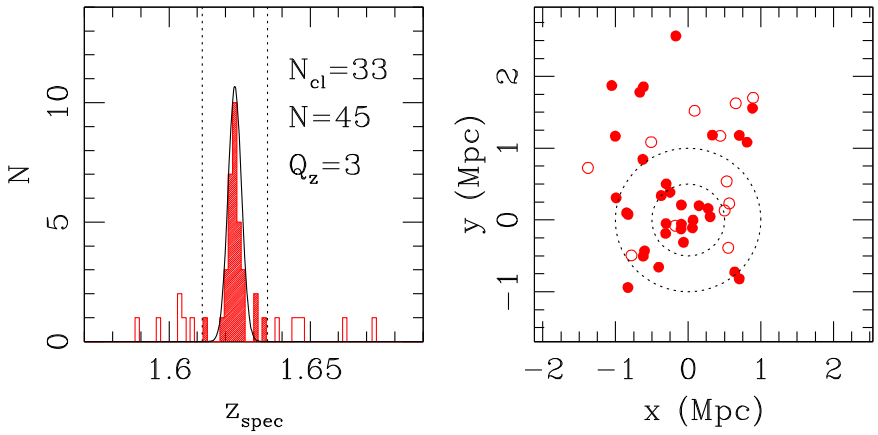

Figure 2. Galaxy cluster IRC 0218's redshift range (left panel) is determined by bootstrapping the 45 galaxies at $1.58 < z_{\rm spec} < 1.68$. We measure the cluster's median redshift and velocity dispersion to be $z_{\rm cl} = 1.6233 \pm 0.0003$ and $\sigma_{\rm cl} = 254 \pm 50$ km s^{-1}; the latter is shown as a Gaussian curve. The cluster redshift range is defined by $\pm 3\sigma_{\rm cl}$ (left panel, dotted vertical lines) which isolates 33 emission-line members (filled histograms). The spatial distribution of the confirmed cluster members is shown in the right panel (filled circles); galaxies outside the cluster redshift range (open histogram) are shown as open circles. At $z = 1.62$, the projected angular scale is 8.471 kpc per arcsec; the large dotted circles correspond to projected (proper) radii at $z = 1.62$ of 0.5 and 1 Mpc.

For our analysis of star formation and gas metallicities, we use the narrow redshift range of $1.6118 < z_{\rm spec} < 1.6348$ defined by our kinematic analysis (Section 3.1) and exclude the cluster galaxies that are X-ray detected (1) and that host broad-line AGN (1; identified by Hα and [N II]); this leaves 26 star-forming cluster galaxies with Hα fluxes and a stellar mass range of $\log(M_\star/M_\odot) = 9.2$–$10.9$ (Table 1). We consider measurements for both individual galaxies as well as for stacked spectra divided into three stellar mass bins.

To stack the spectra, we first divide the 26 star-forming members into three stellar mass bins with ranges of $\log(M_\star/M_\odot) = 9.2$–$9.6$ (9 members), $\log(M_\star/M_\odot) = 9.6$–$10.2$ (9 members), and $\log(M_\star/M_\odot) = 10.2$–$10.9$ (8 members). We normalize the individual galaxies by their Hα flux to give them equal weight (e.g., Sanders et al. 2015), convert the spectra to rest-frame values, combine the spectra, and then measure the line fluxes by fitting Gaussian profiles. Confidence intervals for the line fluxes are determined by boot-strapping the 1D spectra. The stacked spectra show even the weaker emission lines Hβ and [N II] as well as the [S II] doublet (Figure 3).

2.6. Stellar Masses and Stellar Attenuation

To determine stellar masses ($M_\star$) and stellar attenuation ($A_{V,\rm star,SB}$; Table 1), we use the catalog of the UDS field from Quadri et al. (2012) with our spectroscopic redshifts. Both $M_\star$ and $A_{V,\rm star,SB}$ are determined by using FAST (Kriek et al. 2009) to fit Spectral Energy Distributions (SEDs) to the multi-wavelength imaging. We use a Chabrier (2003) initial stellar mass function, constant solar metallicity, and exponentially declining SFR ($\tau = 10$ Myr to 10 Gyr).

We also use FAST to determine the corresponding errors for $M_\star$ and $A_{V,\rm star,SB}$; the latter assumes $R_V = 4.05$ (starburst attenuation curve; Calzetti et al. 2000).[16] FAST determines confidence intervals by using Monte Carlo simulations and modifying the observed fluxes by their photometric errors in each simulation. Note that there are degeneracies between stellar attenuation, star formation histories, metallicities, and dust laws calculated by FAST. These degeneracies can sometimes be broken by independently measuring, e.g., nebular attenuation. For a subsample of the galaxies, we measure both Hα and Hβ emission to determine the Balmer decrement and thus compare nebular to stellar attenuation (Section 3.2).

[16] The starburst (SB) attenuation curve is commonly referred to as the Calzetti law and is appropriate for continuum measurements. We use "starburst" as requested by D. Calzetti.

3. ANALYSIS

3.1. Galaxy Cluster Kinematics

Our combined LRIS and MOSFIRE spectroscopic survey confirms 109 unique objects with redshift quality flag $Q_z = 3$; of these, 9 are stars. We identify 45 galaxies at $1.58 < z_{\rm spec} < 1.68$ and the galaxy cluster is a well-defined peak in the redshift distribution at $z \sim 1.6$ (Figure 1, bottom). To determine the cluster redshift and redshift range, we first need to identify the members. We remove outliers iteratively using a MAD; the MAD is less sensitive to outliers that can be problematic for dynamically young systems such as IRC 0218. For a Gaussian distribution, $\sigma \approx 1.48 \times$ MAD and we use 3σ limits to define the redshift range. We employ five iterations and find a stable solution requires only two iterations: IRC 0218 has 33 members within $1.6118 < z_{\rm spec} < 1.6348$ which corresponds to limits defined by $\pm 3\sigma$ (Figure 2).

To determine IRC 0218's redshift, we bootstrap the 33 galaxies (15000 realizations; Beers et al. 1990) and measure a median cluster redshift of $z_{\rm cl} = 1.6233 \pm 0.0003$ and mean cluster redshift of 1.6232 ± 0.0004. The cluster galaxies have a strikingly narrow redshift distribution and the cluster velocity dispersion (from the bootstrapped distribution) is correspondingly low: $\sigma_{\rm cl} = 254 \pm 50$ km s^{-1}, i.e., more like a group than a fully developed galaxy cluster (see Section 4.1). Figure 2 (right) shows that most (20/33) of the cluster members are within $R_{\rm proj} < 1$ Mpc of the BCG. If we consider only the members at $R_{\rm proj} < 0.5$ Mpc, the cluster redshift and velocity dispersion are virtually identical. The combination of high spatial density and low velocity dispersion are very conducive to galaxy–galaxy merging (Rudnick et al. 2012; Lotz et al. 2013), i.e., frequency and duration of galaxy–galaxy interations is higher than in a field environment.

IRC 0218's redshift and velocity dispersion do not change significantly if we limit our analysis to either the MOSFIRE or LRIS observations only. If we repeat our analysis using only

Table 1
Properties of Hα-detected IRC 0218 Members[a]

Keck ID	α (2000)	δ (2000)	I mag	z_{spec}	$\log(M_*/M_\odot)$	$A_{V,star,SB}$	fHα[b]	fHβ[b]	f[N II][b]	SFR($H\alpha_{star}$)[c]
36395	34.61690	−5.20299	24.70	1.613	$9.41^{+0.18}_{-0.08}$	$0.2^{+0.3}_{-0.2}$	1.8 ± 0.1	0.0 ± 0.6	0.4 ± 0.3	2.2
36849	34.56660	−5.19900	25.00	1.624	$9.60^{+0.07}_{-0.15}$	$0.1^{+0.3}_{-0.1}$	3.4 ± 0.2	0.9 ± 0.4	0.2 ± 0.2	3.6
37269	34.56870	−5.19590	24.72	1.624	$10.39^{+0.05}_{-0.11}$	$0.1^{+0.5}_{-0.1}$	5.1 ± 0.5	0.4 ± 0.5	0.8 ± 0.3	5.3
37522	34.60300	−5.19369	24.95	1.622	$10.20^{+0.17}_{-0.07}$	$1.1^{+0.2}_{-0.5}$	2.1 ± 0.2	0.4 ± 0.3	0.7 ± 0.1	8.1
38080	34.61000	−5.18868	24.15	1.625	$10.34^{+0.00}_{-0.14}$	$0.1^{+0.2}_{-0.1}$	10.3 ± 0.2	2.6 ± 0.5	1.6 ± 0.2	11.0
38455	34.60940	−5.18625	24.02	1.623	$10.87^{+0.02}_{-0.08}$	$0.8^{+0.1}_{-0.2}$	4.6 ± 0.2	1.2 ± 0.3	0.8 ± 0.2	12.2
39150	34.59990	−5.17829	25.50	1.624	$9.22^{+0.14}_{-0.06}$	$0.2^{+0.3}_{-0.2}$	2.3 ± 0.1	0.3 ± 0.5	0.4 ± 0.1	2.8
39463	34.59290	−5.17625	24.23	1.622	$9.57^{+0.05}_{-0.10}$	$0.1^{+0.1}_{-0.1}$	8.7 ± 0.2	1.7 ± 0.6	0.7 ± 0.1	9.2
39771	34.59280	−5.17402	24.36	1.623	$9.81^{+0.07}_{-0.16}$	$0.6^{+0.2}_{-0.2}$	4.9 ± 0.3	1.3 ± 0.4	1.6 ± 0.2	10.1
39989	34.58750	−5.17219	25.28	1.623	$10.29^{+0.10}_{-0.05}$	$0.2^{+0.8}_{-0.2}$	3.6 ± 0.3	0.0 ± 0.3	2.5 ± 0.3	4.3
40243	34.61680	−5.16958	24.78	1.622	$9.61^{+0.07}_{-0.05}$	$0.2^{+0.2}_{-0.2}$	2.4 ± 0.2	0.3 ± 0.5	0.4 ± 0.1	2.8
40382	34.61750	−5.16884	25.18	1.623	$10.05^{+0.08}_{-0.15}$	$1.4^{+0.2}_{-0.2}$	5.3 ± 0.2	1.1 ± 0.3	1.1 ± 0.2	30.8
40568	34.58070	−5.16690	24.79	1.626	$9.49^{+0.08}_{-0.05}$	$0.0^{+0.3}_{-0.0}$	6.7 ± 0.3	1.4 ± 0.2	0.8 ± 0.1	6.2
40729	34.58480	−5.16558	24.76	1.627	$9.49^{+0.01}_{-0.12}$	$0.1^{+0.2}_{-0.1}$	2.0 ± 0.4	0.2 ± 0.4	0.0 ± 0.1	2.1
40731	34.59280	−5.16529	24.84	1.625	$9.25^{+0.04}_{-0.13}$	$0.0^{+0.3}_{-0.0}$	2.7 ± 0.1	2.2 ± 0.7	0.5 ± 0.2	2.5
41189	34.62220	−5.16206	23.77	1.623	$9.78^{+0.09}_{-0.05}$	$0.2^{+0.2}_{-0.2}$	9.0 ± 0.5	2.8 ± 0.3	1.4 ± 0.2	10.9
41297	34.60190	−5.16097	24.44	1.622	$9.93^{+0.11}_{-0.16}$	$0.8^{+0.2}_{-0.2}$	5.3 ± 0.3	0.5 ± 0.4	0.8 ± 0.1	14.0
41548	34.59790	−5.15948	24.48	1.624	$10.50^{+0.15}_{-0.15}$	$1.0^{+0.3}_{-0.3}$	7.3 ± 0.3	0.1 ± 0.5	2.0 ± 0.3	25.1
41956	34.59960	−5.15566	23.75	1.621	$10.25^{+0.05}_{-0.01}$	$1.0^{+0.1}_{-0.2}$	14.6 ± 0.4	2.6 ± 0.8	4.3 ± 0.2	50.2
43178	34.61020	−5.14441	24.66	1.621	$10.47^{+0.13}_{-0.30}$	$1.2^{+0.6}_{-0.3}$	5.4 ± 0.3	1.1 ± 0.5	2.0 ± 0.2	24.3
44102	34.56320	−5.13659	24.62	1.621	$10.69^{+0.20}_{-0.14}$	$0.4^{+1.4}_{-0.2}$	13.8 ± 0.3	1.0 ± 0.6	4.1 ± 0.2	21.5
44403	34.57880	−5.13336	24.88	1.622	$9.36^{+0.11}_{-0.00}$	$0.2^{+0.2}_{-0.2}$	4.9 ± 0.3	2.0 ± 0.6	0.3 ± 0.1	5.9
44459	34.62260	−5.13383	23.93	1.624	$10.12^{+0.12}_{-0.13}$	$0.4^{+0.3}_{-0.2}$	7.0 ± 0.3	0.2 ± 0.5	0.5 ± 0.3	11.0
44587	34.56660	−5.13347	24.12	1.621	$9.92^{+0.03}_{-0.14}$	$0.5^{+0.2}_{-0.1}$	4.9 ± 0.3	2.2 ± 0.5	0.5 ± 0.1	8.8
45959	34.56070	−5.12105	25.05	1.620	$9.28^{+0.22}_{-0.06}$	$1.6^{+0.0}_{-0.3}$	2.0 ± 0.2	0.3 ± 0.4	0.0 ± 0.1	15.2
46922	34.61150	−5.11372	23.21	1.630	$10.16^{+0.14}_{-0.07}$	$0.4^{+0.3}_{-0.1}$	14.9 ± 0.4	4.2 ± 0.4	5.7 ± 0.3	23.6

Notes.
[a] IRC 0218 members ($1.6118 < z_{spec} < 1.6348$; see Section 3.1) that have Hα emission as measured with MOSFIRE.
[b] Observed fluxes in units of 10^{-17} erg s^{-1} cm^{-2}. Note that in several cases, fHβ and f[N II] are upper limits considering the S/N.
[c] Hα fluxes are corrected for dust using $A_{V,star}$ (Equation (7); see Section 3.2) and then converted to star formation rates using the relation from Hao et al. (2011).

the MOSFIRE redshifts, there are 30 members: the median cluster redshift remain the same and the velocity dispersion decreases slightly to $\sigma_{cl,MOS} = 220 \pm 43$ km s^{-1}. Using only the LRIS redshifts, there are 17 members: the median cluster redshift remains the same and the velocity dispersion increases slightly to $\sigma_{cl,LRIS} = 305 \pm 118$ km s^{-1}.

3.2. Balmer Decrement and Attenuation

For a subset of MOSFIRE-detected galaxies, we are able to measure both Hβ and Hα and thus directly determine their internal extinction via the Balmer decrement. Hα is by far the stronger line (Figure 3) where Hα/Hβ = 2.86 is the intrinsic line flux ratio for Case B recombination with electron temperature $T_e = 10^4$ K and electron density of $n_e = 100$ cm^{-3} (Osterbrock 1989). In addition to being weaker, at $z \sim 1.6$ the Hβ line falls in a region of telluric absorption ($\lambda_{obs} \sim 1.264$ μm) which makes it even more challenging to measure.

Only 12 cluster galaxies meet our selection criteria of Hβ $\geqslant 0.5 \times 10^{-17}$ erg s^{-1} cm^{-2} measured at $\geqslant 3\sigma$ significance (Figure 4, left). There are nine cluster galaxies with Hα/Hβ $\geqslant 2.86$ and three members with lesser values that are within $\sim 1-2\sigma$ of this ratio (Figure 4, left). The latter are likely to have negligible attenuation and so we set their attenuation to zero.

The total attenuation curve is parameterized by

$$R_V \equiv \frac{A_V}{E(B-V)} \quad (1)$$

$$k(\lambda) = \frac{A(\lambda)}{E(B-V)} \quad (2)$$

where $A(\lambda)$ is the total magnitude of the extinction at wavelength λ and $E(B-V)$ is the color excess as measured by nebular lines or the stellar continuum. For galaxies with a measured Balmer decrement, the color excess is determined directly from the observed line fluxes with

$$E(B-V)_{H\,II} = [k(H\beta) - k(H\alpha)]^{-1}\, 2.5 \log_{10}\left(\frac{H\alpha/H\beta}{2.86}\right). \quad (3)$$

Using the Cardelli et al. (1989; CCM) attenuation curve for the diffuse interstellar medium where $R_V = 3.1$, $k(H\alpha) = 2.53$, and $k(H\beta) = 3.61$, the color excess is then

$$E(B-V)_{H\,II} = 2.33 \log_{10}\left(\frac{H\alpha/H\beta}{2.86}\right). \quad (4)$$

Figure 4 (right) compares the color excess of the ionized gas $E(B-V)_{H\,II}$ to that of the stellar population $E(B-V)_{star}$; the

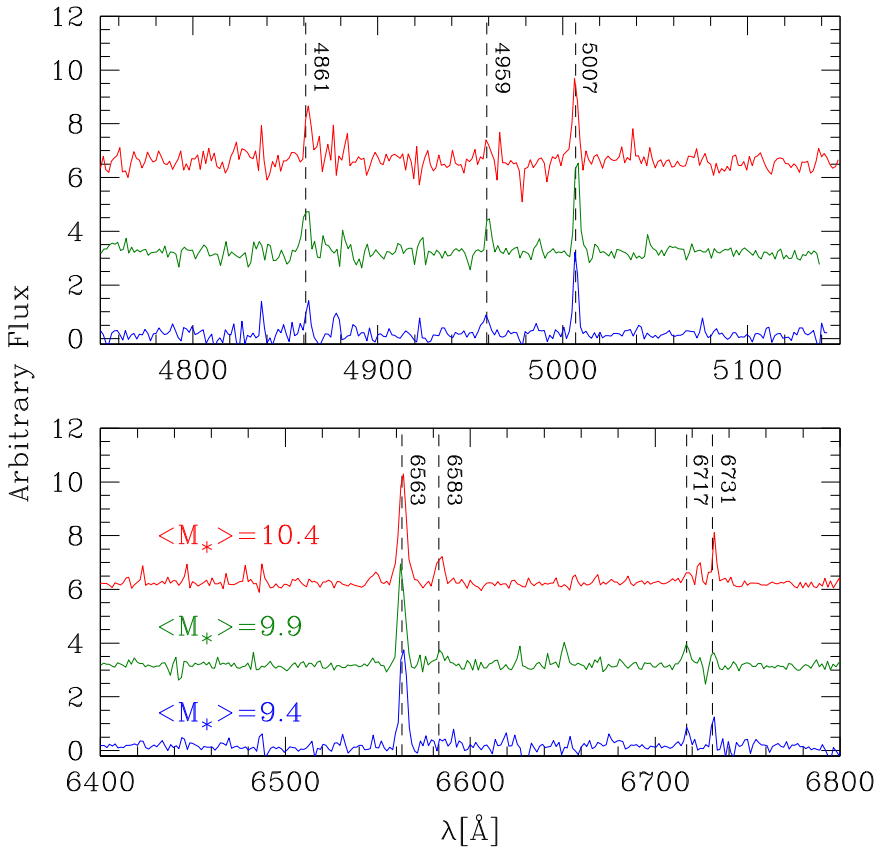

Figure 3. We divide the 26 H$\alpha\lambda$6563 Å-detected cluster galaxies into three separate mass bins and stack their spectra; for clarity, the stacked spectra are smoothed and offset in flux. The stellar mass range is $\log(M_\star/M_\odot) = 9.2$–$10.9$ (Table 2) and the median stellar mass for each bin is included in the figure; from low to high mass bin, there are 9, 9, and 8 members. The individual spectra are first normalized by the Hα flux and converted to rest-frame values, and then the median is taken. At $z_{\rm cl} = 1.6233$, the spectral range corresponding to MOSFIRE includes H$\beta\lambda$4861 Å and the [O III]$\lambda\lambda$4959, 5007 Å pair (top; J-band), and Hα, [N II]λ6583 Å, and the [S II]$\lambda\lambda$6717, 6731 Å pair (bottom; H-band).

latter is determined by fitting to the (UV) stellar continuum with FAST (solar metallicity) and assuming $R_{V,\rm SB} = 4.05$ (Calzetti et al. 2000). For the error in $E(B-V)_{\rm H\,II}$, we add the Hα and Hβ line flux errors in quadrature. For the cluster galaxies, the nebular $E(B-V)_{\rm H\,II}$ is larger than that of the stellar component $E(B-V)_{star,SB}$. This is consistent with results at $z \sim 0$ and $z \sim 1.4$ that support a ratio of $E(B-V)_{\rm star}$ to $E(B-V)_{\rm H\,II}$ of 0.44 (Calzetti et al. 2000; Price et al. 2014). However, we note the large scatter in this ratio that mirrors results from recent studies of field galaxies at $z \sim 2$ (Reddy et al. 2015). Although it is tempting to measure this ratio using the cluster galaxies, our limited sample does not allow us to confirm nor exclude the ratio of 0.44.

Figure 5 (left) shows the cluster galaxies that satisfy our rigorous Hβ criteria and compares their nebular attenuation to stellar mass. The members do not define a correlation between $A(\rm H\alpha)_{\rm H\,II}$ and $M_\star$, in contrast to results at $z \sim 0.1$ (Garn & Best 2010) and $z \sim 1.4$ (Price et al. 2014), nor is any trend visible when we stack the spectra into three mass bins.

The cluster galaxies define a clearer trend between stellar attenuation $A_{V,\rm star,SB}$ as measured by FAST (Figure 5, right) and $M_\star$. The least-squares fit to the 20 members[17] is

$$A_{V,\rm star,SB} = 0.48\log\left[M_*/M_\odot\right] - 4.36 \quad (5)$$

where $\sigma_{\rm rms} = 0.34$. A fit using only the 9 members with a measured Balmer decrement is identical. The relation between $A_{V,\rm star,SB}$ and $M_\star$ seems to be shallower than measured for the field at $z \sim 1.4$ (Price et al. 2014), but there is large scatter.

How then can we correct our Hα fluxes for attenuation given that for most of the Hα-detected galaxies, we only have the stellar attenuation $A_{V,\rm star,SB}$ measured by FAST? For simplicity, we first correct the Hα line fluxes using the nebular attenuation curve from Cardelli et al. (1989) with $R_V = 3.1$

$$A(\rm H\alpha)_{\rm HII} = 2.53 \times E(B-V)_{\rm HII}. \quad (6)$$

We then use the observed stellar to nebular attenuation ratio of $E(B-V)_{\rm star} = 0.44 \times E(B-V)_{\rm H\,II}$ (Calzetti et al. 2000) and the stellar attenuation $A_{V,\rm star,SB}$ as measured by FAST for all of the galaxies where $E(B-V)_{\rm star} = A_{V,\rm star,SB}/4.05$ (see also Steidel et al. 2014)

$$A(\rm H\alpha)_{\rm HII} = 5.75 \times E(B-V)_{\rm star}. \quad (7)$$

We use Equation (7) to correct all of the Hα fluxes for attenuation and determine corresponding SFR. Recently Reddy et al. (2015) measure $R_V = 2.505$ for field galaxies at $z \sim 2$, a value that is lower than the R_V for the starburst and diffuse ISM attenuation curves. However, we cannot discriminate between these models given our limited cluster sample.

[17] We exclude X-ray and broad-line AGN from the fit and also member 45959 whose SED fit indicates a very dusty low-mass galaxy (see Table 1).

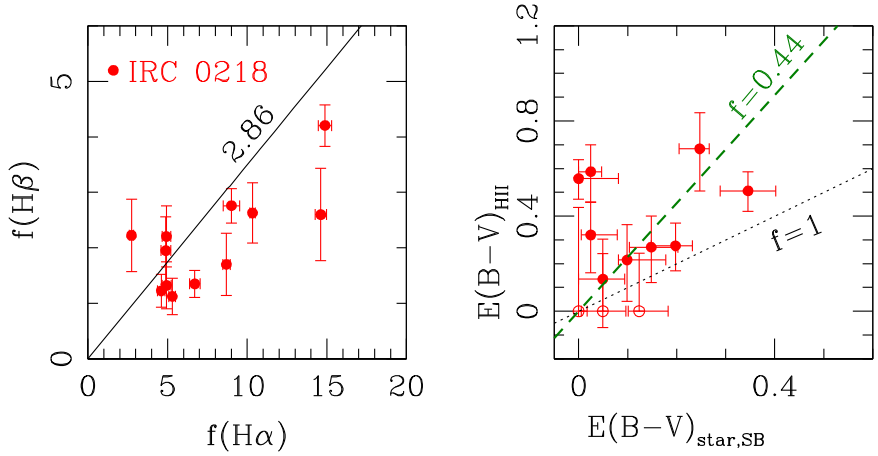

Figure 4. Left: distribution of Hα vs. Hβ line fluxes ($\times 10^{-17}$ erg s^{-1} cm^{-2}) as measured with MOSFIRE where the diagonal line corresponds to Hα/H$\beta = 2.86$ (Balmer decrement for Case B recombination). Our requirement of H$\beta \geqslant 0.5 \times 10^{-17}$ erg s^{-1} cm^{-2} measured at $\geqslant 3\sigma$ confidence identifies 12 cluster galaxies (filled circles); included are the 1σ errors determined from propagating the error spectra. The attenuation for the the three cluster galaxies with Hα/H$\beta < 2.86$ is likely negligible and so we set their Balmer decrement to 0. Right: the color excess measured using the Balmer decrement compared to the color excess from the stellar continuum measured with FAST; we include only the nine cluster galaxies with Hα/H$\beta \geqslant 2.86$ and use the CCM89 reddening law to calculate the nebular $E(B-V)$. For reference, we include the ratio of stellar to nebular $E(B-V)$ measured for local starburst galaxies where the color excess for stars is less ($f = 0.44$, dashed line; Calzetti et al. 2000). The cluster galaxies at $z \sim 1.6$ follow this general trend, but there is signicant scatter that mirrors recent results based on larger samples of field galaxies (see Reddy et al. 2015).

3.3. Hα SFR

To determine Hα SFR, we correct for attenuation using $E(B-V)_{\rm star}$ (Equation (7)) and convert the Hα fluxes to SFR using the relation from Hao et al. (2011):

$$\log\left[{\rm SFR}\left(H\alpha_{\rm star}\right)\right] = \log\left[L\left(H\alpha_{\rm star}\right)\right] - 41.27. \quad (8)$$

This relation assumes a Kroupa IMF (0.1–100 $M_\odot$; Kroupa 2001), but the relation for a Chabrier IMF is virtually identical (difference of 0.05). The uncorrected Hα fluxes of the 26 star-forming members range from 1.8 to 14.9 $\times$ 10^{-17} erg s^{-1} cm^{-2}. Using $E(B-V)_{\rm star}$ to correct for attenuation, the corresponding Hα SFR are 2–50 $M_\odot$ yr^{-1} (Table 1). We have excluded X-ray detected members and broad-line AGN.

The cluster field was imaged with Spitzer MIPS as part of the legacy UKIDSS Ultra Deep Survey (SpUDS PI: J. Dunlop) and the catalog includes all sources detected with S/N > 5 which corresponds to a flux of $\sim$40 μ Jy. The 24 μm fluxes are converted to total infrared luminosities ($L_{\rm IR}$) using the Chary & Elbaz (2001) templates, and SFRs are calculated from $L_{\rm IR}$ using the prescription of Kennicutt (1998), adjusted to the Chabrier IMF. We are able to measure 24 μm fluxes for the six cluster members with the highest Hα ($>$20 $M_\odot$ yr^{-1}).

Even with correcting for dust attenuation, the H$\alpha_{\rm star}$ SFRs are lower compared to the 24 μm SFRs: on average, the 24 μm SFRs for the six detected members (42–155 $M_\odot$ yr^{-1}) are a factor of $\sim$3 larger. The advantage of using Hα is that we are significantly more sensitive, i.e., we can measure SFRs to $\sim$2 $M_\odot$ yr^{-1} compared to $\sim$40 $M_\odot$ yr^{-1} with the 24 μm observations, and thus we are not limited to only the most strongly star-forming dust-obscured cluster galaxies. Papovich et al. (2007) also showed that for galaxies at $z \sim 2$, SFRs based on Chary & Elbaz (2001) templates fit only to 24 μm are larger by $\sim$2–5 compared to SFRs based on a combination 24 μm, 70 μm, and 160 μm. This is intriguingly consistent with the offset we measure when comparing our H$\alpha_{\rm star}$ SFRs to the 24 μm SFRs.

We confirm the original measurement by Tran et al. (2010) of an elevated SFR within the cluster core: the integrated H$\alpha_{\rm star}$ SFR per square Mpc at $R_{\rm proj} < 0.25$ Mpc is about six times higher than at $R_{\rm proj} < 2$ Mpc (Figure 6; Table 2). The five star-forming members at $R_{\rm proj} < 0.25$ Mpc have stellar masses of $\log(M_\star/M_\odot) = 9.3$–$10.3$. The cluster galaxies also show increasing SFR with stellar mass (Figure 7). We stress that the integrated H$\alpha_{\rm star}$ SFRs are lower limits because (1) for the six members with both H$\alpha_{\rm star}$ and 24 μm SFRs, the 24 μm values are on average $\sim$3 times higher; and (2) the limited spatial coverage of the NIR spectroscopy combined with the increasing contamination by field galaxies means we identify fewer Hα-emitting members at larger $R_{\rm proj}$. In Section 4.4, we compare in detail the cluster H$\alpha_{\rm star}$ SFRs to that measured for the field at $z \sim 2$.

3.4. Gas Phase Metallicities

Following several recent analyses on gas metallicities in the field (Kulas et al. 2013; Steidel et al. 2014; Sanders et al. 2015), we measure the oxygen abundance for the cluster galaxies using the N2 method calibrated by Pettini & Pagel (2004):

$$12 + \log({\rm O/H})_{\rm N2} = 8.90 + 0.57 \times \log([{\rm N\,II}]/{\rm H}\alpha). \quad (9)$$

We use only N2 to measure gas metallicities due to our limited ability to measure Hβ and [O III] for individual galaxies. We exclude X-ray detected members and broad-line AGN; we also follow Sanders et al. (2015) and require that $\log([{\rm N\,II}]/{\rm H}\alpha) < -0.3$ to remove potential AGN which removes one member. From our sample of Hα-detected cluster galaxies, we measure N2 for the 20 members where the [N II] emission line is detected at (S/N) > 2; note that [N II] is much weaker than Hα. For five additional members, we place 1σ upper limits on N2. We also measure gas metallicities for the binned spectra (Figure 3).

The cluster galaxies show increasing metallicity with mass (Figures 8 and 9), a trend that is consistent with the mass–metallicity relation (MZR) measured for star-forming galaxies at $z \sim 0$ (Moustakas et al. 2011). The cluster galaxies lie below the local MZR, i.e., the cluster galaxies at $z \sim 1.6$ have lower gas metallicities at a given stellar mass. The offset in the cluster

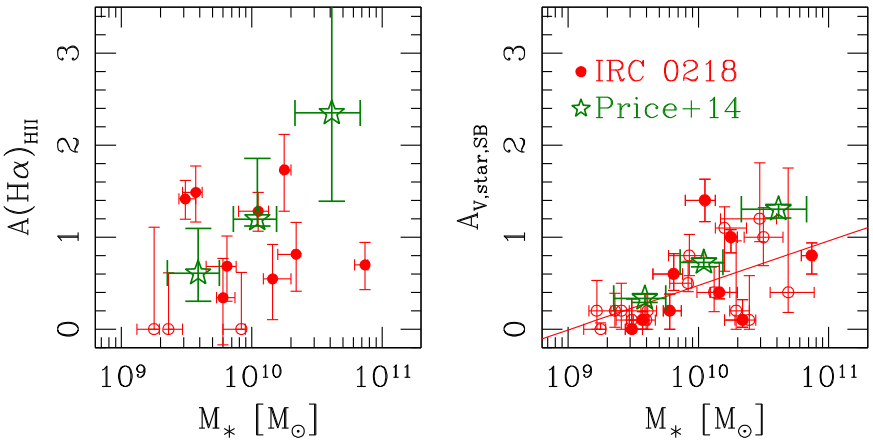

Figure 5. Nebular (left) and stellar (right) attenuation vs. stellar mass for individual cluster galaxies with measured Balmer decrement (filled circles) and $A_{V,\mathrm{star,SB}}$ only (open circles). Shown for comparison are the stacked values for the nebular (left) and stellar (right) attenuation of the field at $z \sim 1.4$ (open stars; Price et al. 2014). The IRC 0218 galaxies do not show any trend between nebular attenuation $A(\mathrm{H}\alpha)_{\mathrm{H\,II}}$ and stellar mass; this is also true when stacking the cluster spectra. In contrast, the cluster galaxies do increase in stellar attenuation $A_{V,\mathrm{star,SB}}$ with $M_\star$ as confirmed with a least-squares fit (diagonal line), but the cluster has a shallower slope than in the field (see also Reddy et al. 2015).

MZR is similar to that observed for field star-forming galaxies at $z \sim 1.6$ (Zahid et al. 2014) at $z \sim 2.3$ (Steidel et al. 2014; Sanders et al. 2015).

4. RESULTS

4.1. Is IRC 0218 A Galaxy Cluster?

IRC 0218 is one of only a handful of galaxy clusters at $z > 1.5$ with a measured cluster velocity dispersion σ_{cl}. The challenge lies in obtaining medium-resolution near-infrared spectroscopy for a sufficient number of members to measure accurate redshifts and map the cluster's kinematic structure (see 3.1). Although NIR spectroscopy is strongly biased toward emission-line galaxies due to the faintness of the stellar continuum, this may be advantageous given the increased star formation at this epoch (e.g., Tran et al. 2010; Brodwin et al. 2013). Note that while cluster studies at $z \sim 2$ using *HST*/WFC3 grism observations can confirm both active and passive members via, e.g., the D4000 break (Gobat et al. 2013; Newman et al. 2014), the grisms' redshift accuracy of $(1+z) \times 1000\,\mathrm{km\,s^{-1}}$ leads to rather uncertain measurements of the cluster velocity dispersion, e.g., Mei et al. (2015).

Using Hα to identify 15 emission-line members, Bayliss et al. (2014) measure a very large velocity dispersion of $1500 \pm 520\,\mathrm{km\,s^{-1}}$ in a galaxy cluster at $z = 1.48$. In comparison, the velocity dispersions of $\sim$750–850 $\mathrm{km\,s^{-1}}$ measured for two proto-clusters at $z = 2.2$ and 2.5 (Shimakawa et al. 2014) are more in line with those of lower redshift clusters, e.g., EDisCS (Milvang-Jensen et al. 2008). The smallest velocity dispersion observed thus far at $z \sim 2$ is for the COSMOS cluster with $\sigma_{\mathrm{cl}} = 552 \pm 52\,\mathrm{km\,s^{-1}}$(Yuan et al. 2014); this cluster also has the most confirmed members (>50) as identified by our ZFIRE survey.

Relative to these studies, IRC 0218's velocity dispersion of $\sigma_{\mathrm{cl}} = 254 \pm 50\,\mathrm{km\,s^{-1}}$ (33 emission-line members; Figure 2) is by far the smallest. This low velocity dispersion is more in the range of galaxy groups than a galaxy cluster (e.g., Gerke et al. 2005; Tanaka et al. 2013). However, this velocity dispersion is consistent with X-ray results: the cluster velocity dispersion corresponding to the total cluster mass of $M_{200} = 7.7 \pm 3.8 \times 10^{13}\,M_\odot$ estimated from the weak X-ray signal detected with *XMM-Newton* (2.3σ level detection; Pierre et al. 2012) is $\sigma_{\mathrm{cl,X\text{-}ray}} \sim 360 \pm 90\,\mathrm{km\,s^{-1}}$, i.e., the dynamical velocity dispersion is consistent with the X-ray derived estimate at $\sim 1.5\sigma$. These values also are consistent with predictions from numerical simulations, e.g., Evrard et al. (2008) show that a halo with X-ray mass of $M_{200} \sim 7.7 \times 10^{13}\,M_\odot$ has an estimated velocity dispersion of $400\,\mathrm{km\,s^{-1}}$. Note that the cluster members are spatially concentrated with 20 of the 33 members within $R_{\mathrm{proj}} = 1$ Mpc of the BCG (Figure 2, right).

Using the Millenium simulation with a semi-analytic galaxy formation model, Shattow et al. (2013) select 50 central galaxies in halos with masses greater than $7 \times 10^{13}\,M_\odot$ and track them from $z = 6$ to $z = 0$; note that this halo mass is essentially IRC 0218's dynamical mass as measured by both kinematics and X-ray. The study finds that by $z = 0$, most of the halos have masses $>2 \times 10^{14}\,M_\odot$, i.e., they are likely to be clusters if not the most massive ones (see also Chiang et al. 2013). Thus IRC 0218 will evolve into a galaxy cluster that can be as massive as the Virgo cluster (Schindler et al. 1999) and possibly as massive as $10^{15}\,M_\odot$.

4.2. Nebular Versus Stellar Attenuation

$E(B-V)_{\mathrm{H\,II}}$ and $E(B-V)_{\mathrm{star}}$ can be used to determine dust properties, i.e., $E(B-V)_{\mathrm{H\,II}}$ probes sightlines to regions of ionized gas that are heated by short-lived OB stars while $E(B-V)_{\mathrm{star}}$ is a measure of the (UV) dust attenuation of the stars and integrated over longer timescales (>100 Myr). For local starbursts, $E(B-V)_{\mathrm{star}}$ and $E(B-V)_{\mathrm{H\,II}}$ are correlated such that the color excess of the stellar continuum is about half that of the ionized gas ($f = 0.44$; Calzetti et al. 2000), i.e., the attenuation as measured by the nebular lines is larger. It is unclear if this relation holds at $z > 1$ with studies measuring ratios varying from $\sim$0.26−1 (Erb et al. 2006b; Yoshikawa et al. 2010; Kashino et al. 2013; Price et al. 2014; Zahid et al. 2014; Reddy et al. 2015).

We are able to directly measure the color excess $E(B-V)_{\mathrm{H\,II}}$ for nine cluster galaxies where $\mathrm{H}\alpha/\mathrm{H}\beta > 2.86$ and $\mathrm{H}\beta \geqslant 0.5 \times 10^{-17}\,\mathrm{erg\,s^{-1}\,cm^{-2}}$ is detected at $\geqslant 3\sigma$ (Figure 4, right). Both $E(B-V)_{\mathrm{H\,II}}$ and $E(B-V)_{\mathrm{star}}$ span

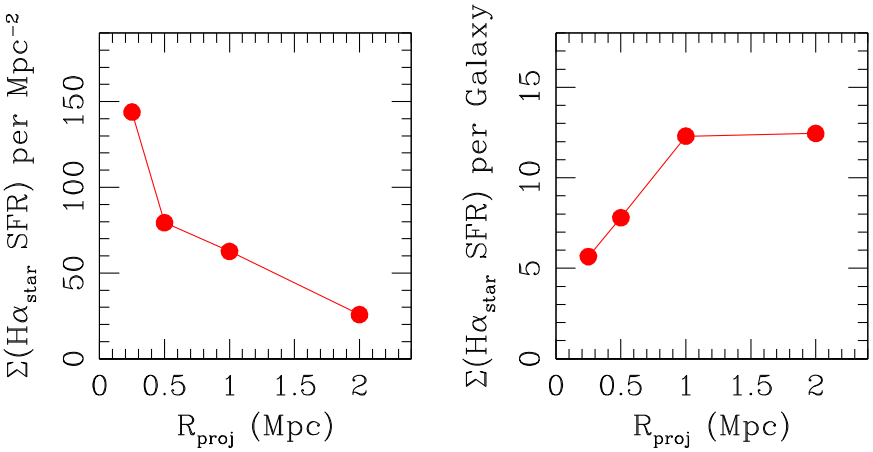

Figure 6. Integrated H$\alpha_{\rm star}$ star formation rate per unit area (the total $M_\odot$ yr^{-1} per square Mpc) is highest in the cluster core ($R_{\rm proj} < 0.25$ Mpc; left) and decreases with increasing cluster radius (e.g., Tran et al. 2010; Brodwin et al. 2013). This is driven by the existence of star-forming members in the core, but the *average* H$\alpha_{\rm star}$ SFR per galaxy is actually lowest in the cluster core and plateaus at $R_{\rm proj} \gtrsim 1$ Mpc (right; Table 2). The propagated errors due to the uncertainty in the Hα line fluxes are smaller than the points ($\pm$0.6–1.4 $M_\odot$ yr^{-1}).

Table 2
H$\alpha_{\rm star}$ Star Formation Rates vs. Cluster Radius

$R_{\rm proj}$	$N_{\rm gal}$	Σ(Hα SFR)[a]	Σ(Hα SFR) per galaxy[b]	$\langle$SSFR$\rangle$ [c]	Σ(Hα SFR) per Area
250 kpc	5	28 $M_\odot$ yr^{-1}	5.6 $M_\odot$ yr^{-1}	0.8 Gyr^{-1}	144 $M_\odot$ yr^{-1} Mpc^{-2}
500 kpc	8	62 $M_\odot$ yr^{-1}	7.8 $M_\odot$ yr^{-1}	0.9 Gyr^{-1}	79 $M_\odot$ yr^{-1} Mpc^{-2}
1 Mpc	16	197 $M_\odot$ yr^{-1}	12.3 $M_\odot$ yr^{-1}	0.8 Gyr^{-1}	63 $M_\odot$ yr^{-1} Mpc^{-2}
<2 Mpc	26	324 $M_\odot$ yr^{-1}	12.5 $M_\odot$ yr^{-1}	0.9 Gyr^{-1}	26 $M_\odot$ yr^{-1} Mpc^{-2}

Notes.
[a] The total enclosed Hα star formation rate corrected for attenuation using $E(B-V)_{\rm star}$ (see Section 3.2). X-ray detected members and broad-line AGN are excluded. Given spectroscopic incompleteness at larger radii, we consider these to be lower limits on IRC 0218's total SFR.
[b] The integrated H$\alpha_{\rm star}$ SFR divided by the number of Hα-detected galaxies within $R_{\rm proj}$; quiescent members are excluded.
[c] The specific star formation rate determined by summing the H$\alpha_{\rm star}$ SFR and $M_\star$ for the Hα-detected members within $R_{\rm proj}$; quiescent members are excluded.

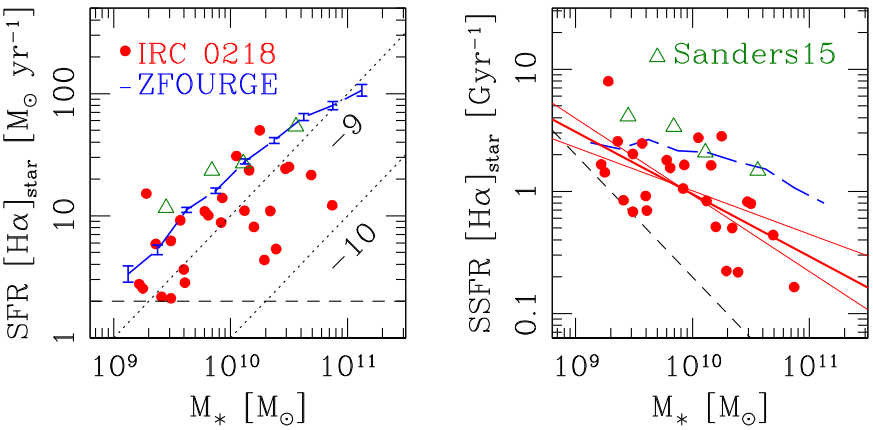

Figure 7. 26 cluster galaxies tend to have lower H$\alpha_{\rm star}$ star formation rates (left) and specific SFRs (right) at a given stellar mass compared to their field counterparts. Left: the H$\alpha_{\rm star}$ SFRs for the cluster galaxies (filled circles) are corrected for extinction using $E(B-V)_{\rm star}$ and typical errors in H$\alpha_{\rm star}$ SFRs and $M_\star$ are $\sim$0.1–0.2 dex (see Section 3.2; Table 1). Included are lines of constant specific star formation rates (SSFR; $M_\odot$ yr^{-1} per $M_\star$; dotted lines) and the horizontal dashed line is our lower SFR limit. For comparison, we include the binned points measured by MOSDEF for Hα-detected field galaxies at $z \sim 2.3$ (open triangles; Sanders et al. 2015) and the star-forming field galaxies at $1.5 < z < 2.0$ from ZFOURGE (long-dashed curve; Tomczak et al. 2015; UV+MIR SFRs). The ZFOURGE errors represent uncertainty in the mean and the stellar mass bins are 0.25 dex. Right: the higher mass cluster galaxies tend to have lower SSFRs compared to their field counterparts in both ZFOURGE (long-dashed curve) and MOSDEF; a least-squares fit to the IRC 0218 members with SFRs > 2 $M_\odot$ yr^{-1} (solid line; 1σ range shown as thin lines) measures a slope that is steeper than in ZFOURGE. The dashed diagonal line shows the SSFR limit corresponding to our SFR limit of 2 $M_\odot$ yr^{-1}.

ranges (0–0.8) that are comparable to values measured at $z \sim$ 1–2 in both field and cluster studies (Zeimann et al. 2013; Price et al. 2014). The ratio of nebular to stellar attenuation is also consistent with the measured values of $\sim$0.44 (Calzetti et al. 2000; Yoshikawa et al. 2010), albeit with considerable scatter.

There is no clear trend between the nebular attenuation $A(\mathrm{H}\alpha)_{\rm H\,II}$ and stellar mass (Figure 5), nor is there any

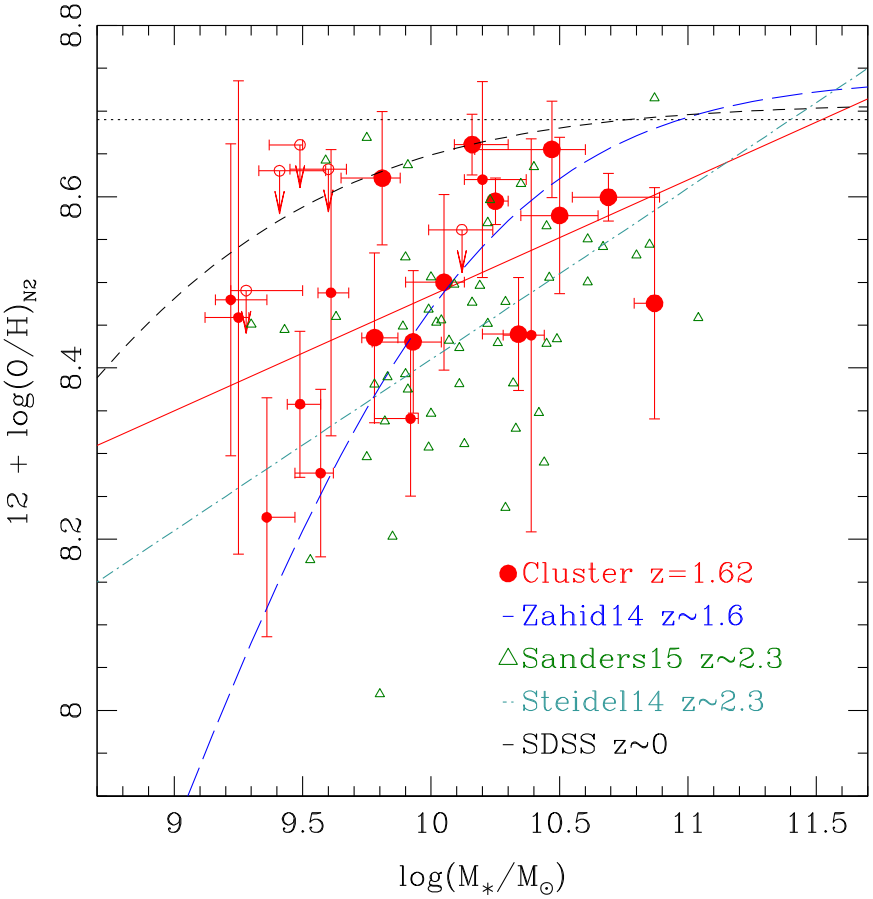

Figure 8. Stellar mass vs. gas metallicity for IRC 0218 members as measured by [N II]/Hα (filled red circles); we fit a least-squares to these galaxies (red line). These cluster galaxies are also divided by SFR[H$\alpha_{\rm star}$] = 10 $M_\odot$ yr^{-1} into low (small filled red circles; 9) and high (large filled red circles; 11) star formation rates. Red open circles (5) with arrows are members with 1σ upper limits on [N II]. Included for comparison are: the MZR of field galaxies at $z \sim 1.6$ in COSMOS (blue long-dashed curve; Zahid et al. 2014); field galaxies at $z \sim 2.3$ from MOSDEF (open green triangles; Sanders et al. 2015); the MZR relation from SDSS (dashed black curve; Moustakas et al. 2011); the linear fit to $z \sim 2.3$ galaxies from (dot–dashed cyan line; Steidel et al. 2014); and solar abundance (dotted line at 8.69; Asplund et al. 2009). The MZR relation for the cluster IRC 0218 (red line) is clearly offset from local galaxies (dashed curve) and agrees with the Steidel fit to galaxies at $z \sim 2.3$ (dot–dashed cyan line).

indication that nebular attenuation depends on environment as suggested by past studies (Koyama et al. 2013b; Zeimann et al. 2013). In contrast, the stellar attenuation $A_{V,\rm star,SB}$ (starburst, $R_V = 4.05$) does increase with stellar mass (Figure 5) but with a slope that is shallower than observed in the field at $z \sim 1.5$ (Price et al. 2014). Our results suggest that the attenuation measured by the integrated stellar light may be less affected by, e.g., patchy dust distribution; however, our sample size is limited. We refer the reader to Reddy et al. (2015) for a more extensive study of dust based on a significantly larger sample of (field) galaxies at $z \sim 2$.

4.3. Star Formation in the Cluster Core

With our sensitive spectroscopic survey of IRC 0218, we measure extinction-corrected H$\alpha_{\rm star}$ SFRs for 26 individual members with ~2–50 $M_\odot$ yr^{-1}; AGN have been removed. Note that an advantage of spectroscopy over using narrow-band imaging to derive H$\alpha_{\rm star}$ SFRs is that we can remove AGNs using [N II]/Hα as well as those detected using X-ray. With the 26 cluster galaxies, the lower limit on IRC 0218's integrated H$\alpha_{\rm star}$ SFR is ~325 $M_\odot$ yr^{-1} (Table 2). The higher integrated H$\alpha_{\rm star}$ SFR in the cluster core (Figure 6) supports our earlier result based on 24 μm observations of IRC 0218 (Tran et al. 2010).

A handful of studies have now also obtained Hα spectroscopy of cluster galaxies at $z \sim 1.5$ using ground-based telescopes and the WFC3 grism in *HST*. Line sensitivities vary, but the consensus is that most galaxy clusters in this redshift range have integrated SFRs within $R_{\rm proj} < 0.5$ Mpc of up to ~200 $M_\odot$ yr^{-1} and SFRs of individual members can be as high as 100 $M_\odot$ yr^{-1} (Hayashi et al. 2011; Zeimann et al. 2013). With an H$\alpha_{\rm star}$ SFR of ~60 $M_\odot$ yr^{-1} integrated within $R_{\rm proj} < 0.5$ Mpc (Table 2), IRC 0218 is consistent with these measurements.

Our analysis uses the integrated H$\alpha_{\rm star}$ SFRs within different $R_{\rm proj}$ (Figure 6; Table 2) to enable direct comparison to the literature. Note that the integrated H$\alpha_{\rm star}$ SFR within $R_{\rm proj}$ is different from the *fraction* of star-forming members. Because the overall galaxy density is higher in clusters, it is possible to have both a large integrated SFR and an increase in quiescent galaxies relative to the field, e.g., Quadri et al. (2012) and Santos et al. (2014). For example, the H$\alpha_{\rm star}$-SFR per square Mpc is highest in the core ($R_{\rm proj} < 0.25$ Mpc), but the average SFR per galaxy is only about half that of galaxies at $R_{\rm proj} < 2$ Mpc (Figure 6).

Our results confirm that the integrated H$\alpha_{\rm star}$ SFRs in the cores of galaxy clusters at $z \gtrsim 1.5$ are significantly higher than in massive galaxy clusters at $z < 1.4$ (Kodama et al. 2004; Finn et al. 2005; Bauer et al. 2011). The astute reader will notice that our H$\alpha_{\rm star}$ SFRs are lower than the 24 μm values

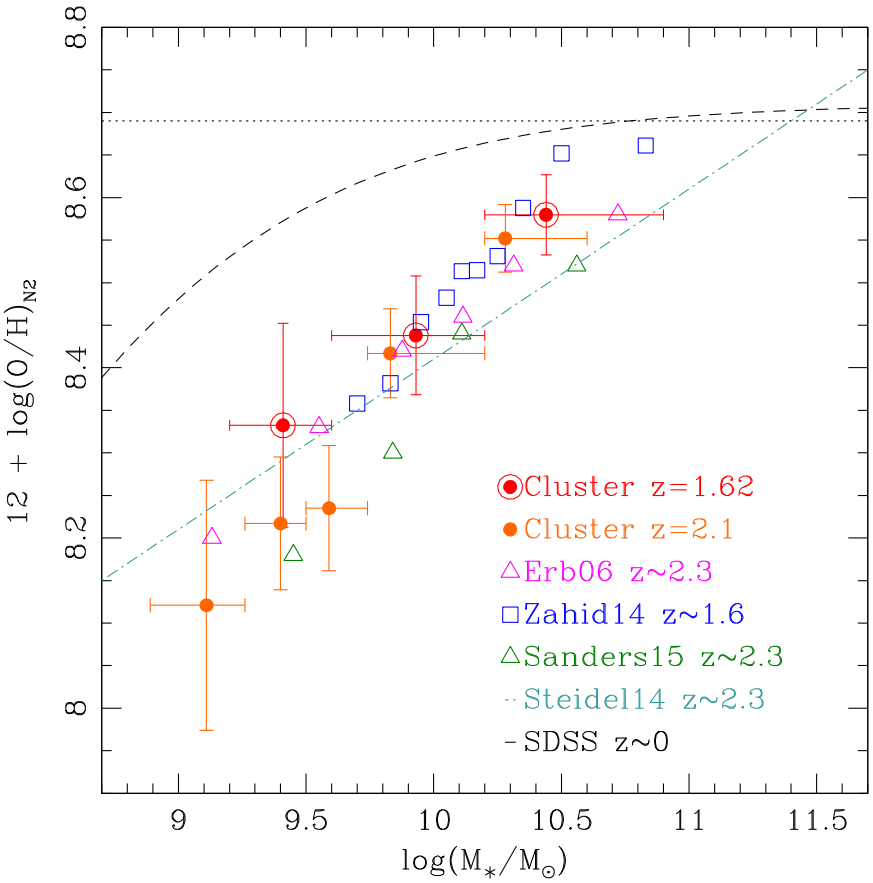

Figure 9. Same as in Figure 8 but for the stacked spectra where the cluster galaxies are divided into three mass bins (large red filled circles; see Figure 3). We show the field data binned in stellar mass from Zahid et al. (2014), Sanders et al. (2015), and Erb et al. (2006a). The IRC 0218 members are remarkably consistent with the field MZR relation at $z \sim 2$ as well as the MZR measured for the COSMOS cluster (filled orange circles; Kacprzak et al. 2015).

published in Tran et al. (2010). For the six IRC 0218 members with both H$\alpha_{\rm star}$ and 24 μm SFRs, the average ratio is $\sim$2.9 $\pm$ 1.1, i.e., the 24 μm SFRs are $\sim$3 times higher. However, it is likely that the 24 μm SFRs are over-estimated: Papovich et al. (2007) showed that for galaxies at $z \sim 2$, SFRs based on Chary & Elbaz (2001) templates fitted only to 24 μm are $\sim$2$-$5 higher compared to SFRs determined with 24 μm, 70 μm, and 160 μm.

We note that if we use the 24 μm measurements for the six Hα-detected members, the the number of cluster galaxies with Hα SFRs $> 30\ M_\odot\ {\rm yr}^{-1}$ increases from two to six. Because we are also constrained by the spatial sampling of the NIR spectroscopy, we consider the H$\alpha_{\rm star}$ SFRs in Table 2 to be lower limits. However, this result is tentative and a larger cluster sample at $z \sim 2$ is needed to better quantify the relation between Hα and 24 μm, especially for SFR $> 20\ M_\odot\ {\rm yr}^{-1}$.

4.4. SFR Versus Stellar Mass

The 26 Hα-detected cluster galaxies have stellar masses of $\sim 10^9$–$10^{11} M_\odot$ and show a trend of increasing SFR with stellar mass that is similar to the field (Figure 7, left), i.e., a "main sequence" of star-forming members (Daddi et al. 2007; Koyama et al. 2013b). Most of the lower-mass cluster galaxies ($M_\star < 10^{10} M_\odot$) will more than double their stellar masses given the elapsed cosmic time since $z = 1.62$ if they maintain their current SSFR (see also Table 2). Our results are consistent with Zeimann et al. (2013) who use WFC3 grism measurements of Hα to show that cluster galaxies at $1 < z < 1.5$ follow an SFR–$M_\star$ relation.

To determine if the SFR–$M_\star$ relation depends on environment, we use the Four-star Galaxy Evolution (ZFOURGE) survey (Tomczak et al. 2014, Straatman et al. 2015) to select star-forming field galaxies at $1.5 < z < 2.0$ with SFRs measured by combining UV and mid-IR fluxes Tomczak et al. 2015). Given our H$\alpha_{\rm star}$ detection limit, we apply a SFR detection threshold of 2 $M_\odot\ {\rm yr}^{-1}$ to both the IRC 0218 and ZFOURGE samples. We compare H$\alpha_{\rm star}$ SFRs and the SSFR (defined to be SFR/$M_\star$) to stellar mass in Figure 7. We also compare to recent results from MOSDEF based on Hα measurements of field galaxies at $z \sim 2.3$ (Sanders et al. 2015).

The IRC 0218 members have systematically lower SFRs compared to the field. However, the difference can be due to using two different methods of measuring SFRs (H$\alpha_{\rm star}$ versus UV+MIR; Kennicutt & Evans 2012). Instead, we consider the slope to test for any environmental difference. By fitting a least-squares to IRC 0218 and bootstrapping the sample (10^4 realizations), we measure the SSFR–$M_\star$ slope to be -0.51 ± 0.30. For the ZFOURGE field galaxies, we measure a shallower slope of -0.23 ± 0.07. The difference in the SSFR–$M_\star$ slope between IRC 0218 and ZFOURGE suggests that environment plays a role, but our results are not statistically significant.

An alternate comparison is to Sanders et al. (2015) who measure Hα SFRs for the field at $z \sim 2.3$ (Figure 7). The IRC 0218 members are clearly offset to lower SFRs compared to the Hα-detected field galaxies. One possible explanation for the lower SFRs in IRC 0218 is the elapsed cosmic time between $z \sim 2.3$ and $z \sim 1.6$ ($\Delta t \sim 1.1$ Gyr). However, the offset in the SFR–$M_\star$ relation for MOSDEF field galaxies at $z \sim 1.6$ at $z \sim 2.3$ (Kriek et al. 2015) is not as significant as observed in IRC 0218. We conclude that our observations indicate a dependence on environment, i.e., lower SFRs in the cluster especially for the higher mass members.

4.5. Gas Phase Metallicity–Mass Relation (MZR)

There is considerable and confusing disagreement over the observed relation between gas phase metallicity and stellar mass (MZR) at $z \sim 2$. While several studies of field and protocluster galaxies find that metallicities increase with stellar mass (Steidel et al. 2014; Zahid et al. 2014; Shimakawa et al. 2015), others do not (Kulas et al. 2013; Stott et al. 2013). Using the N2 method calibrated by Pettini & Pagel (2004), we measure the oxygen abundance in cluster galaxies and compare to their stellar masses (Figures 8 and 9). We find that the IRC 0218 members are offset to lower metallicities relative to star-forming galaxies in the local universe (Tremonti et al. 2004).

The cluster MZR is remarkably similar to that of several field surveys at $z \sim 2$ (Erb et al. 2006a; Steidel et al. 2014; Zahid et al. 2014; Sanders et al. 2015); this is particularly evident when comparing the stacked spectra (Figure 9). To quantify the trend of increasing metallicity with stellar mass, we fit a linear least-squares to the 20 members with measured [N II]/Hα (we exclude the five members with only upper limits on [N II]):

$$12 + \log(\mathrm{O/H})_{\mathrm{N2}} = 8.49 + 0.13\Big[\log\big(M_\star/M_\odot\big) - 10.0\Big] \tag{10}$$

where $\sigma_{\mathrm{rms}} = 0.10$. The MZR in IRC 0218 is comparable to the relation measured by Steidel et al. (2014) for field galaxies at $z \sim 2.3$ where the slope and normalization are (0.2, 8.41). The consistency holds across the full range in mass [$9 \lesssim \log(M_\star/M_\odot) \lesssim 11$]. For these 20 members, the median difference between measured [N II] and that predicted using the fit from Zahid et al. (2014) for field galaxies at $z \sim 1.6$ is only 0.04.

Whether there is an environmental imprint on the MZR at $z \sim 2$ is yet to be clearly established. Ellison et al. (2009) detect a small offset of ∼0.04 dex to higher metallicities in overdense environments at $z \sim 0$ (see also Cooper et al. 2008; Peng & Maiolino 2014), and recent studies at $z \sim 2$ claim to find a measurable offset between their cluster and field samples (Valentino et al. 2014; Shimakawa et al. 2015). However, we find no evidence of an environmental dependence for the MZR when comparing IRC 0218 to the field at $z \sim 1.6$.

What is striking is how the cluster MZR does not evolve at $1.6 < z < 2.1$ (over ∼1 Gyr): IRC 0218's MZR is virtually identical to the COSMOS cluster at $z = 2.1$ (Figure 9; Kacprzak et al. 2015). The similarity of the cluster MZRs matches the essentially constant gas metallicities of lensed field galaxies at $1.5 < z < 2.5$ (Yuan et al. 2013). Our results are also in line with the slow evolution of the MZR predicted by simulations (Davé et al. 2011a), but we note that these same simulations also predict an environmental imprint, e.g., higher metallicities at a given stellar mass, that we do not observe in either galaxy cluster.

Our results show that the cluster MZR and its evolution is indistinguishable from that of the field at $1.6 < z < 2.3$ which is consistent with predictions from recent simulations by Taylor & Kobayashi (2015). We conclude that the somewhat contradictory results observed thus far for the MZR at $z \sim 2$ are due to a combination of different line flux sensitivities and sample sizes of the various studies. By expanding our sensitive survey of cluster galaxies at $z \sim 2$ and comparing to results from MOSDEF (Kriek et al. 2015), we hope to resolve these disagreements.

4.6. SFR and the MZR

Studies at low redshift find that at a given stellar mass, the gas metallicity is lower for galaxies with higher SFR (Mannucci et al. 2010; Andrews & Martini 2013). The Fundamental Mass–Metallicity relation (FMR) quantifies this dependence of the MZR on the SFR and can be explained by a SFR dependence on the ratio of self-enrichment versus inflow of pristine gas. Whether the FMR holds at $z \sim 2$ is unclear with recent studies finding no evidence of an MZR dependence on SFR (Wuyts et al. 2014; Sanders et al. 2015). Evidence for an environmental dependence for the FMR at $z \sim 2.3$ is also tentative at best (Shimakawa et al. 2015).

To test for a dependence on SFR, we divide the IRC 0218 members into approximately equal sized low and high SFR bins (SFR[$\mathrm{H}\alpha_{\mathrm{star}}$] = 10 $M_\odot$ yr^{-1}; Figure 8); we exclude the five members that have only upper limits on their gas metallicities because their true values could be considerably lower. At high stellar masses [$\log(M_\star/M_\odot) > 10$], the high SF members dominate with a metallicity range of ∼0.2 dex. At low stellar masses, the low SF members dominate with a larger metallicity range of ∼0.4 dex.

We fit a least-squares to the 11 high SFR members and the 9 low SFR members with measured [N II] and measure slopes with errors of 0.05 ± 0.08 and 0.10 ± 0.11 respectively. The MZR for both low and high SFR bins are consistent (within 1σ) with that of the cluster sample as a whole as well as the MZR measured by Steidel et al. (2014). We conclude that the IRC 0218 members show no evidence of an MZR dependence on the SFR, but we acknowledge that our cluster sample is limited.

5. EVIDENCE OF ENVIRONMENTAL DEPENDENCE?

With our NIR spectroscopy, we measure Hα and [N II] fluxes that, combined with our SED fits from FAST, provides extinction-corrected Hα SFR, gas phase metallicities from [N II]/Hα, and stellar masses. The primary evidence we find for any environmental dependence is in the cluster SFR. IRC 0218's integrated $\mathrm{H}\alpha_{\mathrm{star}}$ SFR per unit area is about a factor of three higher at $R_{\mathrm{proj}} < 0.25$ Mpc compared to $R_{\mathrm{proj}} < 1$ Mpc (from 144 to 26 $M_\odot$ yr^{-1} Mpc^{-2}; Table 2). This is driven by the higher number density of star-forming galaxies in the cluster core relative to studies of cluster cores at lower redshifts (Tran et al. 2007; Mei et al. 2009). However, the average $\mathrm{H}\alpha_{\mathrm{star}}$ SFR per galaxy is actually lower in the core compared to the values at $R_{\mathrm{proj}} = 0.5$ and 1 Mpc (Table 2; see also Brodwin et al. 2013).

At a given stellar mass, the IRC 0218 members have $\mathrm{H}\alpha_{\mathrm{star}}$ SFRs that are lower compared to the field at $z \sim 2.3$ (Figure 7). The slope of the SFR–$M_\star$ relation also seems to depend on

environment such that the massive cluster galaxies have lower SFRs compared to their field counterparts. The quenching of SF in the massive cluster galaxies at $z \sim 1.6$ means these members will passively age to match their cluster counterparts at $z < 1$ (Mei et al. 2009). The continued stellar growth for lower mass cluster galaxies is also consistent with the more extended star formation histories measured in cluster galaxies at $z < 1$ (Tran et al. 2005a; Tran et al. 2007).

Like field galaxies at $z \sim 1.5$, the cluster galaxies show an increasing amount of attenuation with stellar mass, i.e., more massive galaxies are dustier. This trends hold primarily for the stellar attenuation ($A_{V,\mathrm{star,SB}}$) as measured by the SED fitting to the multi-wavelength photometry (Figure 5). However, the large scatter in both in IRC 0218 and field studies (Yoshikawa et al. 2010; Price et al. 2014) is sobering, particular when comparing the nebular attenuation $A(\mathrm{H}\alpha)_{\mathrm{H\,II}}$ to $M_\star$. It is very likely that the empirical relations used to determine attenuation and thus obtain extinction-corrected SFRs at $z \sim 2$ have uncomfortably large uncertainties and depend on SFRs (e.g., Reddy et al. 2015). A better characterization of dust attenuation laws for difference spectral types at $z > 1$ using essentially low resolution spectroscopy (Kriek & Conroy 2013) holds promise in addressing this issue.

The gas phase metallicity versus $M_\star$ (MZR) for IRC 0218 members is nearly identical to the field at $z \sim 1.6$ (Figures 8 and 9). The cluster MZR does not depend on SFR which is also consistent with field results (Steidel et al. 2014; Wuyts et al. 2014; Sanders et al. 2015). Comparing to our results for the COSMOS cluster at $z = 2.1$ (Kacprzak et al. 2015) shows no evolution in the MZR in the ∼1 Gyr. Our ZFIRE cluster results contradict recent claims at $z \sim 2$ of a measurable difference in the MZR with environment (Kulas et al. 2013; Shimakawa et al. 2015). We note that the environmental imprint on the MZR is small even using SDSS at $z \sim 0$ (Cooper et al. 2008; Ellison et al. 2009; Peng & Maiolino 2014), thus if there is an environmental dependence for the MZR at $z \sim 2$, a considerably larger sample of cluster galaxies is needed to detect it.

Alternatively, calibration issues with using $[\mathrm{N\,II}]/\mathrm{H}\alpha$ to measure gas phase metallicities at $z \sim 2$ may mask any environmental imprint on the MZR. For example, Kewley & Ellison (2008) showed that the choice of line ratios used to measure the gas-phase metallicity has a significant effect on the shape of the MZR. By obtaining the full suite of emission lines for the BPT diagram (Baldwin et al. 1981) to separate star-forming galaxies from those hosting AGN, we can compare to metallicities using alternative line ratios such as $\mathrm{H}\beta/[\mathrm{O\,III}]$(e.g., Shapley et al. 2014). We can also characterize the ionization conditions. If there is a relationship between SSFR and ionization parameter, this would have interesting implications for the properties of star clusters at high redshift, e.g., the spatial distribution and masses of stars embedded within them (Kewley et al. 2015). By expanding our survey of cluster galaxies at $z \sim 2$, we will explore how gas metallicities and ionization parameters are linked to star formation, galaxy (stellar) mass, and environment.

6. CONCLUSIONS

We survey the galaxy cluster IRC 0218 using the multi-object spectrographs LRIS (optical) and MOSFIRE (near-IR) on Keck I. We obtain 130 unique redshifts based mostly on emission lines, e.g., [O II] and Hα, and identify 45 galaxies with $1.58 < z_{\mathrm{spec}} < 1.8$ (Figures 1 and 2). The IRC 0218 members define a narrow redshift distribution with 33 galaxies at $1.6118 < z_{\mathrm{spec}} < 1.6348$. The corresponding cluster redshift and velocity dispersion are $z_{\mathrm{cl}} = 1.6233 \pm 0.0003$ and $\sigma_{\mathrm{cl}} = 254 \pm 50\ \mathrm{km\ s^{-1}}$.

While IRC 0218's velocity dispersion is the lowest measured thus far for a cluster at $z \sim 2$, it is consistent with the σ inferred from the cluster mass estimate of $M_{200} = 7.7 \pm 3.8 \times 10^{13}\ M_\odot$ from the weak X-ray detection (Pierre et al. 2012). Simulations also show that most systems with this velocity dispersion and redshift will evolve into a cluster by $z \sim 0$. IRC 0218 is spatially concentrated with 20 spectroscopically confirmed members within $R_{\mathrm{proj}} < 1$ Mpc of the BCG. The cluster's high spatial concentration and low velocity dispersion are conducive to galaxy–galaxy merging (Rudnick et al. 2012; Lotz et al. 2013).

With MOSFIRE, we reach near-IR line flux sensitivities of $0.3 \times 10^{-17}\ \mathrm{erg\ s^{-1}\ cm^{-2}}$ that, combined with our SED fits to multi-wavelength photometry, provide extinction-corrected Hα SFR, gas phase metallicities using $[\mathrm{N\,II}]/\mathrm{H}\alpha$, and stellar masses. Adopting a $\mathrm{H}\alpha_{\mathrm{star}}$ SFR limit of $2\ M_\odot\ \mathrm{yr^{-1}}$ at $z_{\mathrm{cl}} = 1.6233$ and removing AGNs, we confirm our earlier result based on 24 μm observations of elevated star formation in IRC 0218's core (Tran et al. 2010): the integrated SFR per unit area at $R_{\mathrm{proj}} < 0.25$ Mpc is about a factor of three larger than at $R_{\mathrm{proj}} < 1$ Mpc (Figure 6; Table 2). We consider the $\mathrm{H}\alpha_{\mathrm{star}}$ SFRs to be lower limits due to sparse sampling and because for the handful of objects where we also can measure the Balmer decrement and/or 24 μm flux, the individual SFRs increase by ∼2–3.

In our analysis, the strongest evidence for any environmental dependence at $z \sim 1.6$ is in the cluster SFR. The high $\mathrm{H}\alpha_{\mathrm{star}}$ SFR in the core ($R_{\mathrm{proj}} < 0.25$ Mpc; Figure 6) is driven by the concentration of star-forming members while the average SFR per galaxy in the core is actually half that of galaxies at $R_{\mathrm{proj}} \sim 1$ Mpc (Table 2). The massive cluster galaxies also tend to have lower SFRs compared to their field counterparts (Figure 7). This mass-dependent quenching of SF is needed for these cluster galaxies to match the stellar ages of their cluster counterparts at $z < 1$ (e.g., Tran et al. 2007; Mei et al. 2009).

Like the field, the IRC 0218 members show a trend of increasing attenuation with stellar mass as measured by the SED fits ($A_{V,\mathrm{star,SB}}$), i.e., more massive galaxies are dustier (Figure 5). However, this is not the case when using the nebular attenuation as measured by the Balmer decrement ($A(\mathrm{H}\alpha)_{\mathrm{H\,II}}$). The significant scatter in the nebular attenuation suggests larger problems with correctly measuring dust attenuation at $z \sim 2$ for both cluster and field galaxies (see also Reddy et al. 2015).

The gas phase metallicity versus stellar mass (MZR) for the cluster galaxies is virtually identical to the field at $z \sim 1.6$, and both are offset to lower metallicities compared to galaxies at $z \sim 0$ (Figures 8 and 9). Comparing to the fit determined by Zahid et al. (2014) for field galaxies at $z \sim 1.6$, the median difference between measured and predicted [N II] is only 0.04. Fitting a least squares to the IRC 0218 members confirms that their MZR is the same as for the field as measured by, e.g., Steidel et al. (2014) at $z \sim 2.3$. The cluster MZR does not depend on SFR which is also consistent with recent results on field galaxies (Wuyts et al. 2014; Sanders et al. 2015).

Particularly striking is that IRC 0218 and the COSMOS cluster at $z = 2.1$ (Kacprzak et al. 2015) have the same MZR even though the elapsed time is ∼1 Gyr. Both clusters' MZRs

are also well-matched to the field as measured by several surveys at $z \sim 2$. We do not see any evidence of an environmental imprint on the MZR at $z \sim 2$ as indicated by previous studies (Kulas et al. 2013; Shimakawa et al. 2015). We attribute this difference to our combination of a larger cluster sample with a more sensitive line flux limit.

In summary, environmental effects are likely to be subtle at $z \sim 2$ and require a larger survey of cluster galaxies to fully characterize. With ZFIRE, we are building such a cluster sample and also expanding to include additional line diagnostics needed to test, e.g., the reliability of [N II]/Hα for measuring gas phase metallicity. ZFIRE complements ongoing NIR spectroscopic surveys of field galaxies at $z \sim 2$, e.g., KBSS (Steidel et al. 2014), MOSDEF (Kriek et al. 2015), and KMOS^{3D} (Wisnioski et al. 2015), and will enable us to test for evolution in spatially resolved quantities as a function of environment.

We are grateful to the MOSFIRE team and in particular N. Konidaris for his help throughout the data reduction process. The Keck support staff were equally essential in gathering and processing the MOSFIRE observations with special thanks to M. Kassis, J. Lyke, and G. Wirth. K. Tran thanks M. Kriek, A. Shapley, S. Price, and D. Calzetti for helpful discussions, and R. Sanders for use of their data. This work was supported by a NASA Keck PI Data Award administered by the NASA Exoplanet Science Institute. Data presented herein were obtained at the W. M. Keck Observatory from telescope time allocated to NASA through the agency's scientific partnership with the California Institute of Technology and the University of California. The Observatory was made possible by the generous financial support of the W. M. Keck Foundation. This material is based upon work supported by *HST* GO program #12896 which was provided by NASA through a grant from the Space Telescope Science Institute, which is operated by the Association of Universities for Research in Astronomy, Inc., under NASA contract NAS 5-26555. This material is also based upon work supported by the National Science Foundation under Grant #1410728. GGK acknowledges the support of the Australian Research Council through the award of a Future Fellowship (FT140100933). The authors wish to recognize and acknowledge the very significant cultural role and reverence that the summit of Mauna Kea has always had within the indigenous Hawaiian community. We are most fortunate to have the opportunity to conduct observations from this mountain.

REFERENCES

Andrews, B. H., & Martini, P. 2013, ApJ, 765, 140
Asplund, M., Grevesse, N., Sauval, A. J., & Scott, P. 2009, ARA&A, 47, 481
Baldwin, J. A., Phillips, M. M., & Terlevich, R. 1981, PASP, 93, 5
Bassett, R., Papovich, C., Lotz, J. M., et al. 2013, ApJ, 770, 58
Bauer, A. E., Grützbauch, R., Jørgensen, I., Varela, J., & Bergmann, M. 2011, MNRAS, 411, 2009
Bayliss, M. B., Ashby, M. L. N., Ruel, J., et al. 2014, ApJ, 794, 12
Beers, T. C., Flynn, K., & Gebhardt, K. 1990, AJ, 100, 32
Brammer, G. B., van Dokkum, P. G., Franx, M., et al. 2012, ApJS, 200, 13
Brodwin, M., Stanford, S. A., Gonzalez, A. H., et al. 2013, ApJ, 779, 138
Calzetti, D., Armus, L., Bohlin, R. C., et al. 2000, ApJ, 533, 682
Cardelli, J. A., Clayton, G. C., & Mathis, J. S. 1989, ApJ, 345, 245
Chabrier, G. 2003, PASP, 115, 763
Chary, R., & Elbaz, D. 2001, ApJ, 556, 562
Chiang, Y.-K., Overzier, R., & Gebhardt, K. 2013, ApJ, 779, 127
Cooper, M. C., Tremonti, C. A., Newman, J. A., & Zabludoff, A. I. 2008, MNRAS, 390, 245
Daddi, E., Dickinson, M., Morrison, G., et al. 2007, ApJ, 670, 156
Davé, R., Finlator, K., & Oppenheimer, B. D. 2011a, MNRAS, 416, 1354
Davé, R., Oppenheimer, B. D., & Finlator, K. 2011b, MNRAS, 415, 11
Eisenhardt, P. R. M., Brodwin, M., Gonzalez, A. H., et al. 2008, ApJ, 684, 905
Ellison, S. L., Simard, L., Cowan, N. B., et al. 2009, MNRAS, 396, 1257
Erb, D. K., Shapley, A. E., Pettini, M., et al. 2006a, ApJ, 644, 813
Erb, D. K., Steidel, C. C., Shapley, A. E., et al. 2006b, ApJ, 647, 128
Evrard, A. E., Bialek, J., Busha, M., et al. 2008, ApJ, 672, 122
Finn, R. A., Zaritsky, D., McCarthy, D. W., Jr., et al. 2005, ApJ, 630, 206
Garn, T., & Best, P. N. 2010, MNRAS, 409, 421
Genel, S., Vogelsberger, M., Springel, V., et al. 2014, MNRAS, 445, 175
Gerke, B. F., Newman, J. A., Davis, M., et al. 2005, ApJ, 625, 6
Gobat, R., Strazzullo, V., Daddi, E., et al. 2013, ApJ, 776, 9
Gonzalez, A. H., Stanford, S. A., Brodwin, M., et al. 2012, ApJ, 753, 163
Hao, C.-N., Kennicutt, R. C., Johnson, B. D., et al. 2011, ApJ, 741, 124
Hayashi, M., Kodama, T., Koyama, Y., Tadaki, K.-i., & Tanaka, I. 2011, MNRAS, 415, 2670
Hewett, P. C., Warren, S. J., Leggett, S. K., & Hodgkin, S. T. 2006, MNRAS, 367, 454
Hilton, M., Lloyd-Davies, E., Stanford, S. A., et al. 2010, ApJ, 718, 133
Kacprzak, G., Nanayakkara, T., Yuan, T., et al. 2015, ApJL, 802, L26
Kashino, D., Silverman, J. D., Rodighiero, G., et al. 2013, ApJL, 777, L8
Kelson, D. D. 1998, Ph.D thesis, Univ. California(Santa Cruz, CA: University of California)
Kelson, D. D. 2003, PASP, 115, 688
Kennicutt, R. C. 1998, ARA&A, 36, 189
Kennicutt, R. C., & Evans, N. J. 2012, ARA&A, 50, 531
Kewley, L., Yuan, T., Nanayakkara, T., et al. 2015, ApJ, in press
Kewley, L. J., & Ellison, S. L. 2008, ApJ, 681, 1183
Kimura, M., Maihara, T., Iwamuro, F., et al. 2010, PASJ, 62, 1135
Kodama, T., Balogh, M. L., Smail, I., Bower, R. G., & Nakata, F. 2004, MNRAS, 354, 1103
Koyama, Y., Kodama, T., Tadaki, K.-i., et al. 2013a, MNRAS, 428, 1551
Koyama, Y., Smail, I., Kurk, J., et al. 2013b, MNRAS, 434, 423
Kriek, M., & Conroy, C. 2013, ApJL, 775, L16
Kriek, M., Shapley, A. E., Reddy, N. A., et al. 2015, ApJS, 218, 15
Kriek, M., van Dokkum, P. G., Labbé, I., et al. 2009, ApJ, 700, 221
Kroupa, P. 2001, MNRAS, 322, 231
Kulas, K. R., McLean, I. S., Shapley, A. E., et al. 2013, ApJ, 774, 130
Kurtz, M. J., Mink, D. J., Wyatt, W. F., et al. 1992, in ASP Conf. Ser. 25, Astronomical Data Analysis Software and Systems I, ed. d. M. Worrall, C. Biemesderfer & J. Barnes (San Francisco, CA: ASP), 432
Lawrence, A., Warren, S. J., Almaini, O., et al. 2007, MNRAS, 379, 1599
Lotz, J. M., Papovich, C., Faber, S. M., et al. 2013, ApJ, 773, 154
Mannucci, F., Cresci, G., Maiolino, R., Marconi, A., & Gnerucci, A. 2010, MNRAS, 408, 2115
McLean, I. S., Steidel, C. C., Epps, H. W., et al. 2012, Proc. SPIE, 8446
Mei, S., Holden, B. P., Blakeslee, J. P., et al. 2009, ApJ, 690, 42
Mei, S., Scarlata, C., Pentericci, L., et al. 2015, ApJ, 804, 117
Milvang-Jensen, B., Noll, S., Halliday, C., et al. 2008, A&A, 482, 419
Moustakas, J., Zaritsky, D., Brown, M., et al. 2011, arXiv:1112.3300
Muzzin, A., Wilson, G., Yee, H. K. C., et al. 2012, ApJ, 746, 188
Newman, A. B., Ellis, R. S., Andreon, S., et al. 2014, ApJ, 788, 51
Noeske, K. G., Weiner, B. J., Faber, S. M., et al. 2007, ApJL, 660, L43
Oke, J. B., Cohen, J. G., Carr, M., et al. 1995, PASP, 107, 375
Osterbrock, D. E. 1989, Astrophysics of Gaseous Nebulae and Active Galactic Nuclei (Mills Valley, CA: Univ. Science Books)
Papovich, C., Bassett, R., Lotz, J. M., et al. 2012, ApJ, 750, 93
Papovich, C., Momcheva, I., Willmer, C. N. A., et al. 2010, ApJ, 716, 1503
Papovich, C., Rudnick, G., Le Floc'h, E., et al. 2007, ApJ, 668, 45
Peng, Y.-j., Lilly, S. J., Kovač, K., et al. 2010, ApJ, 721, 193
Peng, Y.-j., & Maiolino, R. 2014, MNRAS, 438, 262
Pettini, M., & Pagel, B. E. J. 2004, MNRAS, 348, L59
Pierre, M., Clerc, N., Maughan, B., et al. 2012, A&A, 540, A4
Popesso, P., Biviano, A., Rodighiero, G., et al. 2012, A&A, 537, A58
Price, S. H., Kriek, M., Brammer, G. B., et al. 2014, ApJ, 788, 86
Quadri, R. F., Williams, R. J., Franx, M., & Hildebrandt, H. 2012, ApJ, 744, 88
Reddy, N. A., Kriek, M., Shapley, A. E., et al. 2015, ApJ, 806, 259
Rudnick, G. H., Tran, K.-V., Papovich, C., Momcheva, I., & Willmer, C. 2012, ApJ, 755, 14
Sanders, R. L., Shapley, A. E., Kriek, M., et al. 2015, ApJ, 799, 138
Santos, J. S., Altieri, B., Tanaka, M., et al. 2014, MNRAS, 438, 2565
Schaye, J., Crain, R. A., Bower, R. G., et al. 2015, MNRAS, 446, 521
Schindler, S., Binggeli, B., & Böhringer, H. 1999, A&A, 343, 420

Shapley, A. E., Reddy, N. A., Kriek, M., et al. 2015, ApJ, 801, 88
Sharples, R., Bender, R., Agudo Berbel, A., et al. 2013, Msngr, 151, 21
Shattow, G. M., Croton, D. J., Skibba, R. A., et al. 2013, MNRAS, 433, 3314
Shimakawa, R., Kodama, T., Tadaki, K.-i., et al. 2014, MNRAS, 441, L1
Shimakawa, R., Kodama, T., Tadaki, K.-i., et al. 2015, MNRAS, 448, 666
Spitler, L. R., Labbé, I., Glazebrook, K., et al. 2012, ApJL, 748, L21
Steidel, C. C., Rudie, G. C., Strom, A. L., et al. 2014, ApJ, 795, 165
Stott, J. P., Sobral, D., Bower, R., et al. 2013, MNRAS, 436, 1130
Straatman, C. M. S., Spitler, C. R., Quadri, R. F., et al. 2015, ApJ, submitted
Tadaki, K.-i., Kodama, T., Ota, K., et al. 2012, MNRAS, 423, 2617
Tanaka, M., Finoguenov, A., Mirkazemi, M., et al. 2013, PASJ, 65, 17
Taylor, P., & Kobayashi, C. 2015, MNRAS, 448, 1835
Tomczak, A. R., Quadri, R. F., Tran, K.-V. H., et al. 2015, ApJ, submitted
Tomczak, A. R., Quadri, R. F., Tran, K.-V. H., et al. 2014, ApJ, 783, 85
Tonnesen, S., & Cen, R. 2014, ApJ, 788, 133
Tran, K., Papovich, C., Saintonge, A., et al. 2010, ApJL, 719, L126
Tran, K. H., van Dokkum, P., Illingworth, G. D., et al. 2005a, ApJ, 619, 134
Tran, K.-V. H., Franx, M., Illingworth, G. D., et al. 2007, ApJ, 661, 750
Tran, K.-V. H., van Dokkum, P., Franx, M., et al. 2005b, ApJL, 627, L25
Tremonti, C. A., Heckman, T. M., Kauffmann, G., et al. 2004, ApJ, 613, 898
Valentino, F., Daddi, E., Strazzullo, V., et al. 2015, ApJ, 801, 132
Wetzel, A. R., Tinker, J. L., & Conroy, C. 2012, MNRAS, 424, 232
Whitaker, K. E., Labbé, I., van Dokkum, P. G., et al. 2011, ApJ, 735, 86
Williams, R. J., Quadri, R. F., Franx, M., van Dokkum, P., & Labbé, I. 2009, ApJ, 691, 1879
Wisnioski, E., Förster Schreiber, N. M., Wuyts, S., et al. 2015, ApJ, 799, 209
Wong, K. C., Tran, K.-V. H., Suyu, S. H., et al. 2014, ApJL, 789, L31
Wuyts, E., Kurk, J., Förster Schreiber, N. M., et al. 2014, ApJL, 789, L40
Yoshikawa, T., Akiyama, M., Kajisawa, M., et al. 2010, ApJ, 718, 112
Yuan, T., Nanayakkara, T., Kacprzak, G. G., et al. 2014, ApJL, 795, L20
Yuan, T.-T., Kewley, L. J., & Richard, J. 2013, ApJ, 763, 9
Zahid, H. J., Kashino, D., Silverman, J. D., et al. 2014, ApJ, 792, 75
Zeimann, G. R., Stanford, S. A., Brodwin, M., et al. 2013, ApJ, 779, 137